The inaudible sound of thunderstorms

Master Thesis

by

Jelle Daniel Assink

October 2006 - June 2007

Supervisors:

Drs. L.G. Evers
Royal Netherlands Meteorological Institute - Department of Seismology

Dr. H. Paulssen
Utrecht University - Department of Seismology

Dr. I. Holleman
Royal Netherlands Meteorological Institute - Department of Weather Research

Contents

Abstract

By measuring infrasound, a wide variety of atmospheric sources can be identified. In this study, infrasound associated with thunderstorm lightning discharges is investigated. For this purpose, infrasound observations are compared with discharge detections based on a electromagnetical (EM) detection system. Both systems are operated by the Royal Netherlands Meteorlogical Institute. The initial reason for carrying out the study is a study concentrating on the validation of the EM detection system by a variety of methods, for both scientific and social purposes.

The main objective of the study is to investigate the detectibility of lightning discharges with infrasound. For this purpose, infrasound detection parameters are compared with discharge detections at different distances to infrasound arrays. These analyses provide results on the detectibility in terms of extent of detection, discrimination between cloud-cloud and cloud-ground discharges and possible localization of discharges with infrasound.

From these analyses, infrasound coherency, apparent velocity, amplitude and spectral content of the observed infrasound appears to be closely related to the distance of lightning discharges to the infrasound array. Current detection techniques limit successful association to distances up to 70-80 km. Moreover, correlations show that cloud-ground discharges can be associated with infrasound mainly; cloud-cloud discharges are not detected or can be associated to low coherent infrasound solely.

In order to provide unambiguous associations of infrasound to lightning discharges, infrasound detections at multiple arrays are compared by crossbearing localization. Localization attempts do not appear to provide satisfactory results yet; the infrasound arrays being capable of detecting thunderstorm signals are too far away to relate the detection results in a meaningful way.

Furthermore, the content and behaviour of associated infrasound is investigated. The form of associated infrasound resembles the blast-waveform and is coherent over the array elements. The blast-waveform is readily associated to cloud-ground discharges. The observed waveform is the key to the interpreted source mechanism.

By picking amplitude values, the attenuation of the associated blastwave as function of distance is investigated. A first-order decaying trend is observed with distance, although the datapoints are relatively scattered. The results are explained in terms of attenuation and source mechanisms.

Lastly, observations on subsonic pressure variations, coupled to thunderstorm fronts are described. Infrasound arrays appear to be succesful in detecting the back-azimuths of propagating fronts.

In conclusion, infrasound observations correlate well with the cloud-ground discharge detections by the EM detection system. Currently, localization by crossbearing is not possible, therefore validation of the EM system is not yet possible. However, future studies may enable localization by enhancing the infrasound detection algorithm and array configurations. Advanced boundary conditions may reduce the scattering in the observed attenuation curves.

Chapter 1

Introduction

1.1 Study objective

The objective of this research is to determine whether one is able to detect discharges from thunderstorms using infrasonic waves and to which extent. The Royal Netherlands Meteorological Institute, KNMI, operates a FLITS (acronym for Flash Localisation by Interferometry and Time of Arrival System) lightning detection system. The system exploits electromagnetic waves emitted from thunderstorms to detect and localize thunderstorm discharges; both VHF and LF antennas are used for this purpose. Thunderstorm discharges can be subdivided in Cloud-Cloud (CC) and Cloud-to-Ground (CG). A more detailed description of the FLITS system is given in section 2.2. The detection of a discharge is dependent on the configuration of the system. In order to calibrate the system properly, it is necessary to compare detections of the FLITS system with detections using alternative techniques, amongst which infrasound, LOFAR (*http://www.lofar.org*) low frequency radio telescope and weather radar; see *Noteboom* (2006).

A pilot study by *Holleman et al.* (2006) was carried out in order to make an inventory of these alternative techniques. This research therefore can be regarded as a follow-up on the infrasound section described in that study. The authors concluded from the pilot study that there is a promising relation between discharges and observed infrasound detection, at least at distances till 40 km. More detailed research on detectibility, content of infrasound related to discharges, source determination, atmospheric wavepropagation modelling and discrimination between CC and CG are further objectives of this study. This chapter will introduce concepts of infrasound, thunder and earlier research in the same field.

1.2 General considerations to infrasound

Sound waves are mechanical waves and propagate through media as longitudinal waves. For longitudinal waves, the particle displacement is in the direction of wave propagation. Important properties of sound waves are frequency, wavelength, velocity and amplitude. Sound wave propagation can be expressed as propagation of alternating pressure. There-

fore, amplitude is expressed in units of pressure (e.g. pascal). Generally, the human ear is able to distinguish these air pressure fluctuations in the frequency band of 20-20,000 Hz. Sound waves above and below this hearing range are referred to as *ultrasound* and *infrasound*, respectively. For infrasound, the lowest frequency of interest is somewhat arbitrary; in principle one can resolve frequencies down to 0 Hz. The technical properties of the instruments exploited therefore determine what the lower passband of infrasound is. For K.N.M.I. instruments, the lower passband is currently at 500 s, but even longer periods may be resolved in future as technical research carries on. The sound wave velocity is dependent on the physical properties of the medium through which the waves pass and is proportional to the square root of the ratio of the elastic modulus and density. In the atmosphere, the speed of sound is approximately 344 m/s, under standard atmospheric conditions.

Several applications make use of sound waves in the inaudible spectrum. For ultrasound, the most classical example is sonar. The advantage of ultrasound is its ability to sample objects with a very short wavelength signal, therefore with high resolution. Infrasonic waves, on the other hand, having a rather low-frequent content, have the advantage of relative insensitivity to attenuation while travelling through a medium. Therefore, infrasonic waves have a longer range than counterparts higher in the sonic spectrum. Clearly, there is a trade-off between resolution and penetration, similar to behaviour of elastic waves in seismic exploration studies. Infrasonic waves may travel over thousands of kilometers, depending on the medium through which the energy travels.

Infrasound is generated in the atmosphere by movement of large volumes of air. The characteristics of infrasonic waves enable us to detect and monitor low-frequent sonic events. Historically, atmospheric infrasound events have been detected on seismographs and misinterpreted as earthquakes. By measuring the low-frequent air pressure oscillations with separate arrays of microbarographs or microphones, one is able to distinguish between atmospheric infrasound events and earthquakes. Moreover, one is able to detect and monitor other major atmospheric events as volcanic eruptions, supersonic planes, exploding meteors, standing ocean waves and explosions. See *Evers and Haak* (2001, 2003, 2005) for a detailed description of detection of these events using infrasound arrays, exploited by the Royal Netherlands Meteorlogical Institute (KNMI). The configuration of the infrasonic array is of major influence on the frequency band of interest. The detection of explosions is of particular interest, especially in the context of nuclear explosion detection. Infrasound is assigned as one of the monitoring techniques in the Comprehensive Nuclear-Test-Ban Treaty (CTBT), which was signed in 1996. Other techniques involve seismics, hydro-acoustics and radio nuclides.

Obviously, an infrasonic array is able to detect a large variety of infrasonic events. It is therefore important to associate the detection with its proper source, especially in cases of (nuclear) explosions. Part of the analysis is carried out by the application of a detection methods and waveform analysis. Current detection techniques at KNMI involve algorithms based upon coherency/variance analysis over array elements (Fisher, *Melton and Bailey* (1957); *Smart and Flinn* (1971)). Other detection methods that are well-known are algorithms as PMCC; see *Cansi* (1995). An earlier study performed at KNMI

showed better detection results for Fisher compared to PMCC, see *Calje* (2005). This study will not take into account other detection mechanisms than Fisher detection, though the author believes in further improvement of the current algorithm. The instrumentation and detection algorithm will be described intensively in section 2.1.1.

Infrasound waves travel throughout the whole atmosphere, a medium which is regarded to be horizontally layered into distinct zones. In figure 1.2.1, a schematic overview is given of the structure of the atmosphere. This layering is based on the temperature distribution across the atmosphere. Zones of constant temperature are therefore referred to as *pauses*. By modelling the velocity structure of the atmosphere, it is possible to model ray propagation through the atmosphere. The approach proposed by *Garcés et al.* (1998) proves to offer robust results in a wide variety of observational studies, e.g *Petit* (2000); *Evers and Haak* (2005).

For this study, the lowermost part of the atmosphere, the troposphere, is of importance; most infrasonic energy will be between clouds and Earth surface. In average, thunderstorm clouds evolve at 3-5 km height; because of discharges, the potential difference between ionosphere (around Stratopause) and Earth surface is maintained. More information on the characteristics of thunderstorms is given in the next section.

1.3 Thunderstorms and discharges

Thunderstorms are part of the atmospheric electrical circuit. The atmosphere is charged with electrons and ions due to cosmic radiation and natural radioactivity. The *ionosphere*, 50 km above the Earth surface is the charged layer of the atmosphere. Consider figure 1.2.1 for a schematic compositional figure of the atmosphere. A constant potential difference of +300,000 V compared to the Earth's surface exists; although the atmosphere is rather resistive, there is a constant leak of current to the Earth surface. One can regard the atmosphere as a condensator. In order to maintain the total current in the atmosphere (1400 A), thunderstorms recharge the ionosphere. Therefore, thunderstorms can be regarded as 'batteries' in the atmospheric electrical circuit and 'feed' in this way the potential difference Earth's surface - ionosphere. Thus, recharge is going hand-in-hand with discharge. Four major types of discharges exist, indexed by the direction and nature of current. For an average CG discharge, the maximum electrical discharge is 30 kA; maximum electrical discharges of 300 kA are observed. The rise time of the CG discharge heavily influences the amount of induction from a discharge. Induction can have interference effects on electrical devices and can even cause defects.

Thunderstorms are very convective storms in general, exhibiting a large separation of positive and negative current. Separation and occurence of irregular distribution of current are major causes of lightning generation, though the exact process describing the generation of electrical charge is yet unclear. Several theories exist but none of them does explain all observed phenomena completely. Considering the discharges; a chain-reaction may occur in thunderstorm clouds, due to generation of small sparks due to irregular distribution. A pre-lightning channel is generated from the chain-reaction. When the field-strength is

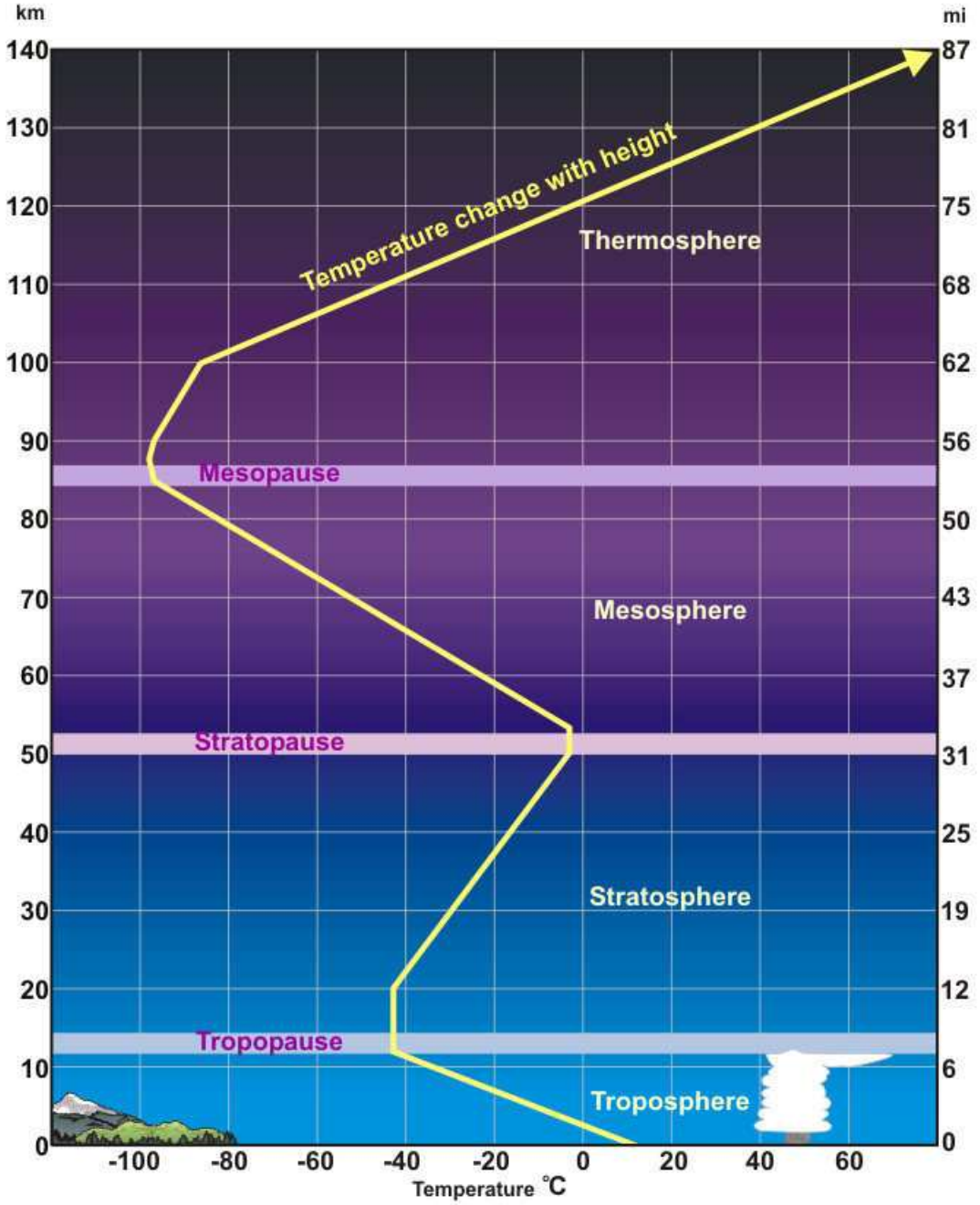

Figure 1.2.1: Atmospheric profile, showing the structure of the atmopshere in various distinct zones. On top, the temperature change with height is plotted with a solid yellow line.

high enough the electrical circuit is then short-circuited and the main discharge takes place (*return stroke*). For a cloud-ground discharge, this happens when the pre-lightning channel is close enough to the Earth surface. Because current can redistribute in a cloud quickly, the process of lightning generation can be repeated several times. What is observed as one discharge, in reality often exists as multiple discharges (observed as blinking lightning). See *Holleman* (2005) for more detailed meteorological information on lightning.

The high temperature of a lightning channel, 30,000 °C, is reached in a short time. This causes the surrounding air to expand so fast that one can regard the expansion as an explosion. Thunder, as the explosion is referred to, travels with the speed of sound, ca. 344 m/s and is popular model to explain observed infrasound; see *Few* (1969); *Beasley et al.* (1976). As mentioned above, infrasonic waves travel over a long range compared to (normal) sonic waves, because the acoustic absorption coefficient is proportional to the square of the frequency. Due to attenuation, a 1 kHz signal will lose 90% of its energy after 7 km travelling at sea level, while for a 1 Hz signal this distance equals 3000 km; see *Bedard* (2005). Provided that thunder has an infrasonic part, it is to be expected that the infrasound will arrive at the arrays from distant thunderstorms and one is able to detect the direction and coherence of thunder for a given thunderstorm using an infrasound array. Two (or more) infrasound arrays will enable the observer to locate thunderstorms using triangularization techniques. Other models, amongst which the electrostatical source mechanism, describing the generation of infrasound due to thunderstorms are to be discussed further in section 1.4.1.

1.4 Earlier research

In literature, several authors have addressed the question whether infrasound emissions are coupled to lightning and thunder. This paragraph summarizes key articles in this field. Several authors have concentrated on the detectibility of severe (thunder)storms with infrasonic signals, similar to this study. However, the meteorlogical context in these articles is somewhat different from the Dutch climate; the areas of investigation are often located in Northern America. In these regions, thunderstorms occur in combination with severe storms and tornadoes. In the Netherlands, thunderstorms are not as severe as in Northern America, although it must be stressed that the atmosphere is definitely not tranquil during thunderstorms. The meteorological conditions in Northern America may be of large influence on the measurements and one may expect to obtain different results in the Netherlands.

Another subject covered in the articles is the description of the source mechanism explaining the generation of infrasound from lightning. Research on this subject is summarized as well. It is important to have an overview of existing models on generation of infrasound by lightning. These models provide insight on the infrasonic waveform and frequency content, important aspects in infrasound processing. In theoretical studies, the source mechanism is modelled and tested by comparing synthetic power spectra of thunder with observed power spectra over the whole acoustic band, while focussing on the infra-

sonic band. Observational studies often address the question of the source mechanism as well, as will be discussed in section 1.4.2

1.4.1 Source mechanism

In *Few* (1969), a *thermally driven expanding channel model* describing acoustic energy emission as a blastwave, is proposed. According to the model, neither cylindrical nor spherical divergence is able to explain the source on its own. Moreover, the author shows that the pressure wave intensity increases by increasing the lightning channel segments; the shape of the power spectrum is unchanged, though. Random variations in energy distributions along the lightning channel and variations in channel tortuosity may broaden the power spectrum. Systematic variations may influence the peak frequency. Because of the relative short time-span of a return stroke, relative to the formation of a pressure wave, it is inferred that in a complex thunderstorm, each return stroke produces its own pressure wave. Therefore, it is concluded that the power spectrum of a complex thunderstorm is expected to equal to the sum of the power spectra of all individual strokes. A broad distribution from below 10 Hz to 150 Hz or even higher is suggested with peak values below 100 Hz. Power spectra of thunderstorms consisting of very different return strokes will contain subsidiary maxima. The dominant peak will usually belong to the first stroke, because of its high energy level. To conclude, in other words: observed infrasound is the low frequency part of the thunder spectrum.

In *Holmes et al.* (1971), the power spectrum is investigated more thoroughly; forty thunder events are analyzed by power spectrum methods. Most spectra show peak power in the frequency region from < 4 to 125 Hz. Difference between CC and CG discharges are observed in terms of peak frequency value. While CC discharges show a mean peak frequency of 28 Hz, CG discharges exhibit a mean peak frequency of 50 Hz. Moreover, the total acoustic energy is higher for CG discharges, as expected. The source mechanism proposed by *Few* (1969) appears to be adequate in describing the dominant frequency pattern for CG discharges, but fails to explain high energy lower frequency peaks of some CG and most CC discharges. The electrostatic mechanism as described in *Dessler* (1973) (originaly Wilson (1920)), is proposed to explain these phenomena.

In *Dessler* (1973), the *electrostatic mechanism* model is further discussed which deals with the generation of a negative pulse following a lightning discharge as atmospheric pressure equilibrium tends to be restored from the region in a thundercloud where charge is removed. This model is evaluated for a layered or a cylindrical cloud region. Estimates on amplitude and peak frequencies are given and are within the range of 0.2-2 Hz. However, the predicted beam is relatively restricted to straight up and down. In *Holmes et al.* (1971); *Barthendu* (1971), the electrostatic source mechanism is further discussed in terms of (infra)sonic power spectra. *Dessler* (1973) predicts a symmetrical pulse with the model; observations in *Balanchandran* (1979) reveal that the rarefaction phase is much larger amplitude that the compressional phase. Therefore, it is suggested that the electrostatical model should be modified in order to explain the observations better.

Lastly, *Balanchandran* (1979) points out that turbulence and oscillations on top of

thunderstorms may be the cause of sound generation. However, turbulence may also reduce the signal-to-noise ratio as non-coherent signal.

A complete understanding of the source mechanism is however not established, as the mechanism is a matter of discussion. Perhaps both mechanisms may provide an adequate explanation of the thunderstorm infrasound generation over the whole infrasonic band. The shockwave model may adequately explain the far-field (CG) features, while the electrostatic model may explain CC discharges best. Joint studies combining meteorology and infrasound may resolve the principal question of thunderstorm infrasound generation. Infrasonic observations in the range of 1-10 Hz are to be given more attention, as *Bowman and Bedard* (1971) points out as well.

1.4.2 Observational studies

Bowman and Bedard (1971) describe observations of subsonic disturbances and infrasound from a variety of severe storms with an array of microbarographs. These observations are coupled with meteorlogical observations and relations are drawn between severe storms and observed pressure deviations. The **subsonic** (i.e. travelling with $v < v_{sound}$) disturbances are described in terms of waveform and propagation path. Local weather reports are used in the study, especially in order to predict travelpaths and arrival times at other array element locations. It is concluded that the subsonic disturbance is quite coherent over large distances and the propagation velocity is constant and the observed disturbances can be related to occuring severe weather. Furthermore, low-frequent **infrasonic** observations are described; it is interpreted that severe storms do radiate infrasound over very large distances ($>$ 1000 km). As observed at long ranges, the travelpath and waveform may deviate due to occuring winds and meteorlogical conditions. Moreover, multi-array detection of one storm enable the identification of the storm location, radiating infrasound. A study by Young et al. (1968) is summarized as well, in which is observed that within 40 miles the direction of observed infrasound coincides with the location of a thunderstorm system. From this study, it is concluded that storm cells with high elevations for radar echotop returns are the source for radiated infrasonic energy.

However, as pointed out by *Bedard* (2005), infrasound is not a common feature of all severe weather. A case study is referred to in which is shown that detected infrasound does not originate from CG discharge locations. Consistency with spectral measurements in other studies is mentioned, putting the energy from lightning discharges in the audible range. The author investigates several source mechanisms that might be responsible for observed infrasound, vortices and boundary layer instabilities. A relation between funnel diameter and pressure variations in the 0.5-10 Hz passband is suggested.

It is noted in *Noble et al.* (unpubl.), that not every thunderstorm produces infrasound signals. Most of the storms that did produce infrasound were very severe and produced intense gust fronts and tornadoes. Infrasound in the passband of 0.2-25 Hz is observed. Peaks in the spectrum are related to the dynamics of the storm. The authors refer to studies that exploit infrasound as a warning system for this kind of storms.

In *Beasley et al.* (1976), an experiment is performed to test the electrostatic source

mechanism and thus the hypothesis that infrasound is generated by lightning. Based upon recordings of time and direction of both infrasound and electromagnetic emissions from severe thunderstorms, the authors show that less than half of the infrasound events show agreement with electromagnetic emissions. The authors suggest that infrasound is emitted in an earlier stage of the storm, since there is a correlation between earlier observed infrasound and later severe storm locations.

Bohannon et al. (1977) report an observation of a single infrasonic low-frequent pulse in the 1 Hz region by an array of 4 microphones recording thunder. The low-frequent pulse arrives just prior to the thunder and it appears that its origin is in the cloud directly over the array. Higher frequency pulses further in the record show larger differential traveltimes over the array elements. It is argued that lightning channel heating is not the source of the pulse because of the observed character of the signal: a rarefaction pulse as described by *Dessler* (1973). Moreover, the pulse occurs only once in the recordings, while lightning channel heating signal is typically multiple in character. Lastly, the signal is observed to be near vertically incident.

In *Balanchandran* (1979), evidence for the presence of strong infrasound signals from a number of thunderstorms is presented. One tripartite array is used to record infrasound in a 0.1-1 Hz passband. The characteristics of the signals are in agreement with the findings by *Dessler* (1973). Observations show vertical incidence, sharp rarefaction pulses and frequencies as low as 0.1 Hz. The sharp main pulse has a dominant frequency of 1.0 Hz and a peak-to-peak amplitude of 10 μbar; low-frequency oscillations follow the main pulse. Although the author acknowledges that the data is presented without simultaneous electric field measurements supporting thunder as source for the infrasound observations, it is stated that all characteristics of the observations point to thunder as the only possible source candidate. Observed infrasonics from nearby storms (negligible effects of meteorological conditions on wave-propagation) show impulsiveness and intermittency that is predicted by an electrostatic mechanism. Furthermore, it is found that the coherency of the signal over the array is relatively low, compared to other sources. This is attributed to the directionality of the signal and the source itself. No infrasound is recorded from thunderstorms not overhead the infrasound array. Relations between infrasound generation, storm dimensions and type of discharges are suggested. The author states that investigating the infrasonic part of thunder enables one to get more insight in the time-dependent spatial charge distribution in a thundercloud and hence more insight in thunderstorm processes.

Somewhat different infrasound observations are described in the publication by *Liszka and Hobara* (2006). The authors describe the detection of infrasonic chirps (few seconds in duration, rising in frequency from 0.5 to 8 Hz) and associate them with a passing thunderstorm. As possible generation mechanism of the infrasonic emission, the sprite is suggested. A sprite is a transient luminous event generally at 55-80 km height in the mesosphere over the thunderstorms with lifetimes of milliseconds to tens of milliseconds. The sprite is predominantly associated with positive ground flashes with a large charge moment change. By triangularization of the signal, the infrasonic source is identified to be coincident with the sharp front of a cloud system, which is capable of generating sprites. By applying an automatic chirp detection algorithm, 100 infrasound chirp events are detected

between 1994 and 2004. Using statistics, the authors argue that the observed chirps are generated from sprites.

A pilot study for validation of KNMI lightning detection system based on electromagnetics involves several methods, amongst which infrasound detections *Holleman et al.* (2006). In a passband of 1.0-20.0 Hz several features are observed that are attributed to electrical discharge and thunder. The observed events correlate very well to detected thunderstorm discharges using the KNMI lightning detection system in time and bearing. From the study, infrasound can be associated over a distance of at least 40 km. This study can be regarded as a follow-up study on the infrasound part of this pilot study.

1.5 Outline of thesis

Following the introduction to the problem of the research, the outline of this thesis will be as follows. Chapter 2 will describe measurements and instrumentation, for both infrasound and FLITS arrays. Moreover, subsequent processing will be described. Chapter 3 will show infrasound observations, compared with FLITS observations and provide interpretations based upon observed detection parameters and waveform characteristics. This is done for both one and multiple arrays. In chapter 4, the observations from the preceding chapter are discussed and interpreted. Chapter 5 summarizes the study and addresses the research objectives, to which extent infrasound can be used to detect thunderstorm discharges and discusses shortcomings and possible further research in this field.

Chapter 2

Measurements & methods

This chapter describes the measurements and methods, used to obtain the results. The chapter is divided in the description of instrumentation and processing of infrasound and the lightning detection system FLITS.

2.1 Infrasound

2.1.1 Instrumentation

Figure 2.1.1 shows the KNMI micobarometer as employed in the different infrasound arrays (see figure 2.1.2). Atmospheric pressure variations can be measured in different ways; both low-frequent microphones and high-frequency barometer are suitable. In designing the KNMI infrasound arrays, microbarometers were used for practical reasons.

The pressure deviation is measured by a differential pressure sensor. This sensor resides beneath the air inlet and measures the incoming pressure with respect to the reference pressure in the backing volume. Because a capillary is added to the backing volume, the sensor only measures pressure fluctuations with respect to the ambient atmospheric pressure. The acoustical resistance of this capillary determines the lower frequency cut-off of the instrument by its diameter and length. The relaxation time of the instrument enables it to measure periods down to 500 s; pressure fluctuations with periods larger than 500 seconds are lead back to the atmosphere. The thick walled backing volume with the capillary inside (instead of outside) garantee temperature stability.

The instruments are mounted beneath the surface in a PVC container; the container has a concrete top. This container stabilizes the instrument's calibration and protects it. To the six container's openings, porous garden hoses are mounted, in order to reduce wind noise. Wind is now sampled over an area instead of a point. Since wind is coherent over small distances, this improves signal-to-noise ratio.

For a more complete description of the instrumentation, consider *Evers* (in prep.).

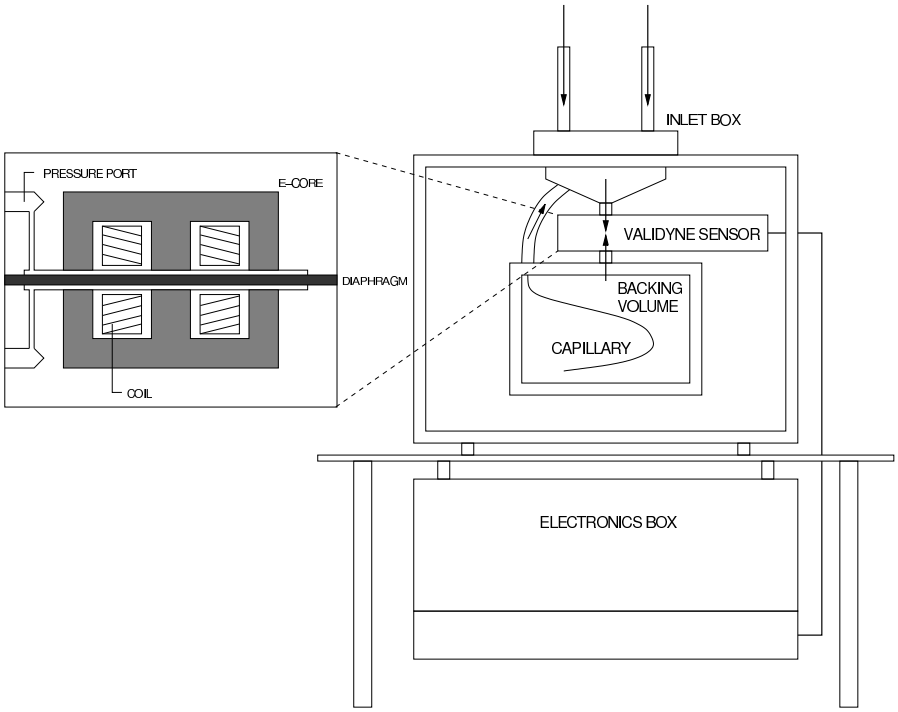

Figure 2.1.1: The microbarometer as deployed by KNMI. Every infrasound array is built up from several of these instruments, mounted beneath the surface in a PVC container. This container stabilizes the instrument's calibration and protects it. Figure adapted from L.G. Evers.

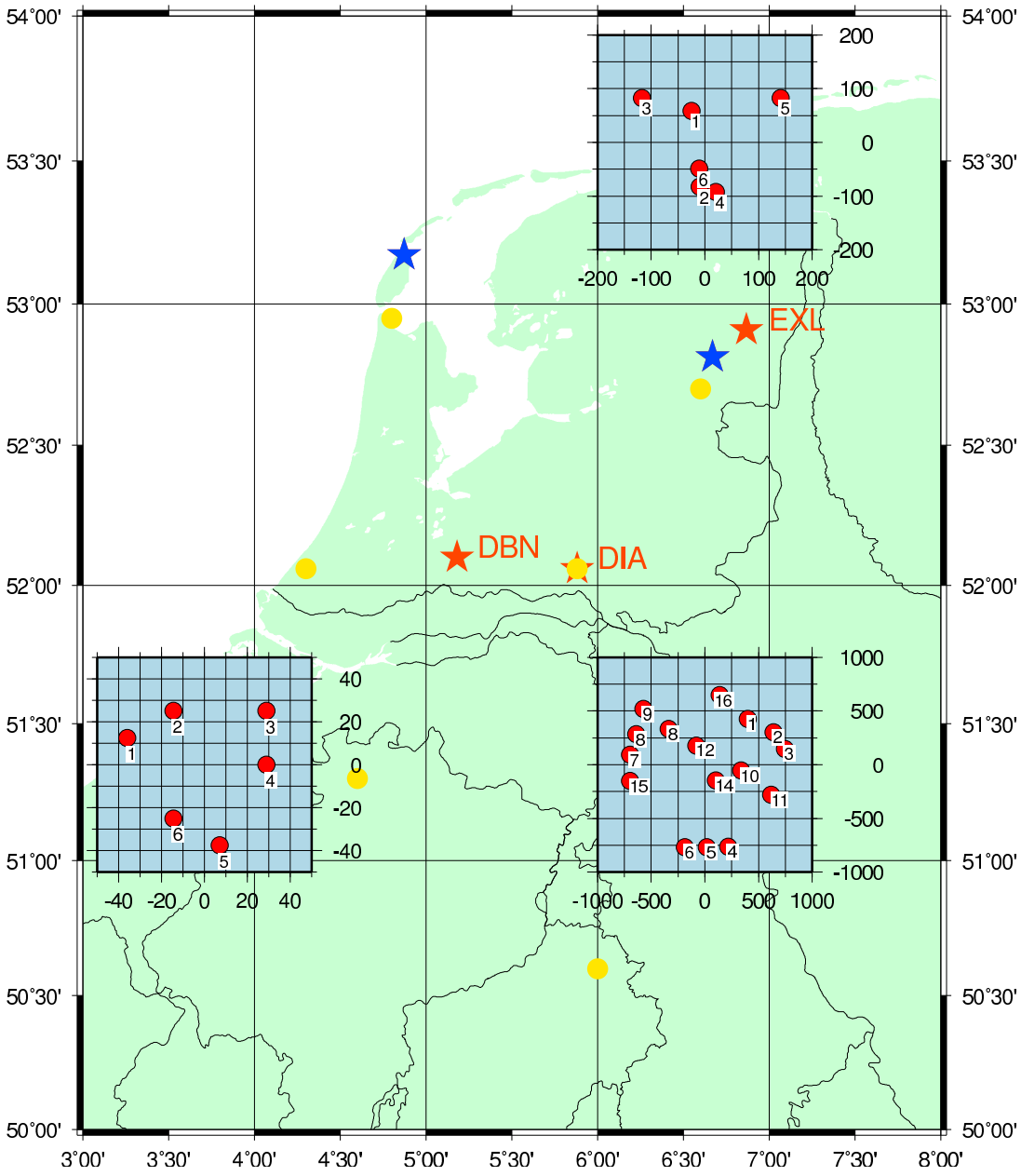

Figure 2.1.2: The locations of all infrasound arrays in the Netherlands. For this study, red-coloured stars refer to infrasound arrays DBN (De Bilt), DIA (Deelen) and EXL (Exloo); these arrays were used for infrasound detections. Their respective array designs are given in a rectangular grid in meterscale. The infrasound arrays coloured with blue stars were not used but plotted for completeness. The FLITS lightning detection network is plotted in this map with yellow circles. For more information on the infrasound arrays and lightning detection network, consider the text in this chapter.

2.1.2 Array layout and response

Figure 2.1.2 shows the KNMI infrasound arrays in The Netherlands. For this study, only the arrays marked with red stars, DBN (De Bilt), DIA (Deelen) and EXL (Exloo), are considered. Arrays are used in many geophysical applications, in order to increase Signal-to-Noise ratio and to be able to locate sources. All arrays have different designs and aperture, as shown in the figure. DBN is the smallest array (aperture 70 m), followed by EXL (aperture 300 m). DIA is by far the largest array, exhibiting an aperture of over 1500 m. Moreover, the lay-out of the arrays is different. The lay-out and aperture controls the array's response; the lay-out is configured such that for a given aperture, an optimal response is obtained.

Array response can be described as the answer you get from the array on the whereabouts of an event. A well configured array will give an adequate answer and provides with a correct slowness vector value. The slowness vector involves information on direction and apparent velocity of the event. This can be expressed mathematically. The basis of all wave phenomena studies lies with the wave equation 2.1.1:

$$\frac{\partial^2 u}{\partial t^2} = \frac{1}{c^2}\nabla^2 u \tag{2.1.1}$$

Solving the equation in 1 dimension, one obtaines a solution for a plane wave in terms of displacement $u(\bar{r}, t)$, equation 2.1.2. The plane wave approximation is widely used in seismology; especially far from source the approximation deviates not much from more realistic spherical wavefronts. Plane waves are furthermore easily visualized and mathematically handled; see e.g. *Sheriff and Geldart* (1995).

$$u(\bar{r}, t) = e^{i\omega(t-\bar{p}\cdot\bar{r})} \tag{2.1.2}$$

In which ω is angular frequency, t is the travel-time dependency and $\bar{p}$ is the slowness vector of the travelling wave; $\bar{r}$ is the position vector of an instrument. There is no time-dependence for a vertically incident plane wave on a horizontal 2D array; therefore, the array response is calculated by considering a vertically incident wave. The array response is mathematically defined as the normalized sum of all measured displacements squared:

$$R(\omega, \bar{p}) = \left| \frac{1}{C} \sum_{j=1}^{C} e^{i\omega(\bar{p}\cdot\bar{r_j})} \right|^2 \tag{2.1.3}$$

In equation 2.1.3, C refers to the number of array elements. The array response $R(\omega, \bar{p})$ can now be plotted by choosing a wave frequency ω and a suitable slowness grid. For infrasonic events, it is important that the slowness grid is defined around possible apparent velocities (speed of sound to infinity) and directions (0°-360°). By choosing an appropriate slowness grid, the response in the infrasonic domain can be calculated, as plotted in figure 2.1.3. In this figure, array responses for a vertically incident plane wave of different frequencies are plotted for the different arrays DBN, DIA and EXL. Comparison of array responses is possible due to the normalization of the sum.

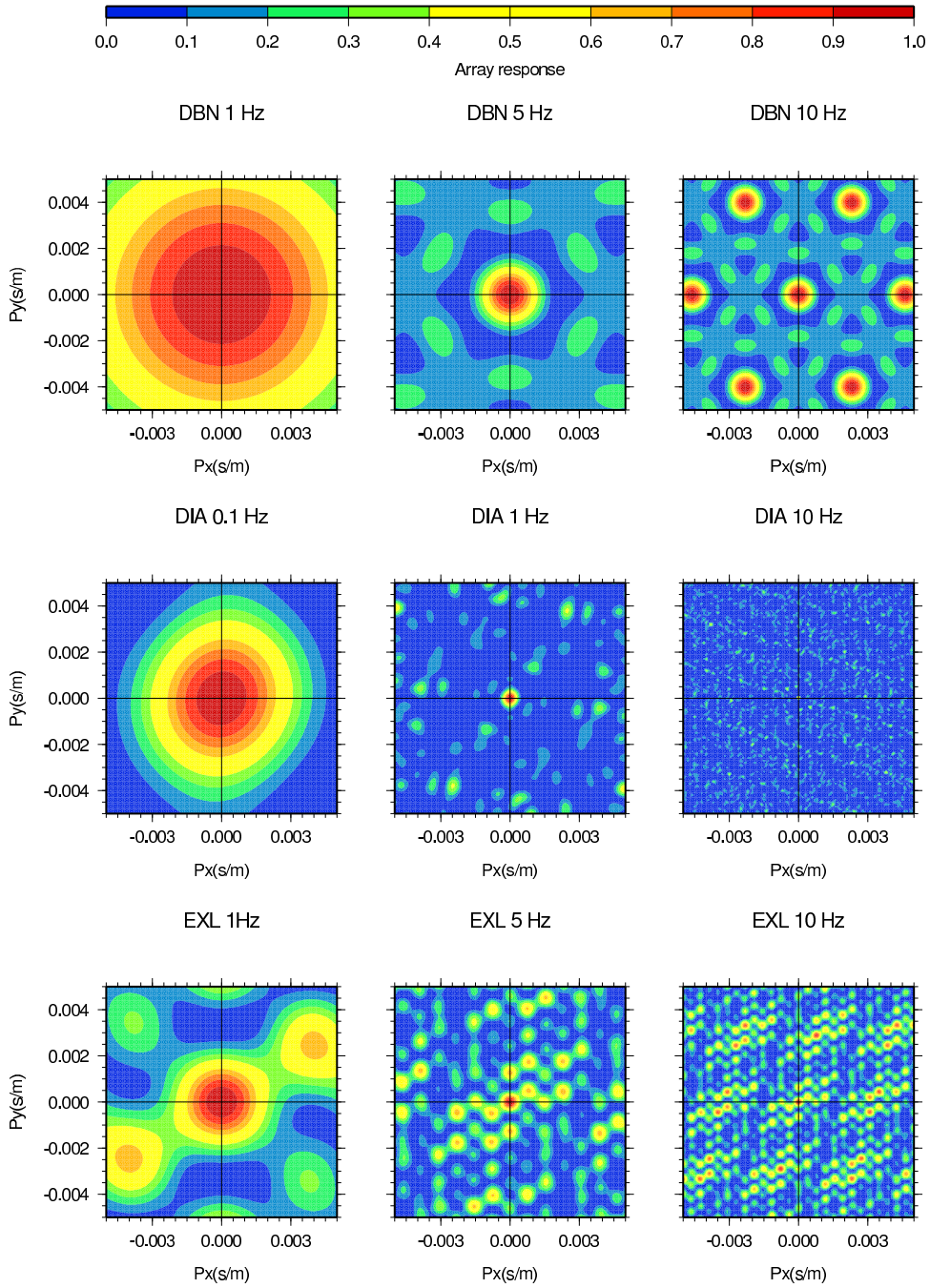

Figure 2.1.3: For each of the infrasound arrays DBN, DIA and EXL, 3 array responses are plotted for vertically incident plane waves at 3 different frequencies. These frequencies lie in the frequency band of interest for infrasound studies. Instead of 5 Hz, a vertical incident wave with $f = 0.1$ Hz is considered for DIA, in order to show the array's sensistivity to lower frequent infrasound because of its larger aperture. DBN and EXL are more similar w.r.t. responses. However, EXL has larger aperture and a different array layout. For array layouts, one is referred to figure 2.1.2

Note the different array responses for the different wave frequencies. The array response is dependent on the array design (i.e. number and location of array elements, inter-station distance) and total aperture. Important aspects of the array response are a circular, peaked main energy lobe in the center of the grid and the low-amplitude sidelobes at distance from the main lobe. The main lobe should - for this case - be in the center of the slowness grid since the wave is vertically incident, giving it zero slowness or infinite velocity. Similarly, the apparent velocity would equal the speed of sound when an infrasonic wave was travelling horizontally over the array. Between real and apparent propagation velocity the following relation holds:

$$v_{app.} = \frac{v_{real}}{\sin\phi} \tag{2.1.4}$$

Where $\sin\phi$ is the angle of incidence. For events with a different incidence and back-azimuth, the main lobe should be concentrated elsewhere in the infrasonic slowness domain.

The main lobe should be circular, in order to reduce array's sensitivity to different directions. Thus, events are detected with the same likelihood, providing equal atmospheric conditions. Furthermore, the main lobe should be peaked, assuring a high-resolution array with small errors in the found slowness vector for a given event. Back azimuth and apparent velocity are given by the slowness vector; see equations 2.1.5-2.1.6; the sharpness of the peak is thus very important in order to resolve the event's whereabouts adequately. Lastly, it is important that sidelobes - if present - are of low energy and are at distance from the main lobe, in order to reduce the chance that events are detected in the regions of the sidelobes (spatial aliasing), with corresponding erroneous slowness vectors; instead, a correct response should concentrate most energy in its main lobe, thereby identifying infrasonic sources with the correct slowness vector.

$$v_{app.} = \frac{1}{|\bar{p}|} = \frac{1}{\sqrt{p_x^2 + p_y^2}} \qquad \textit{apparent velocity} \tag{2.1.5}$$

$$\phi = \tan^{-1}\left\{\frac{p_y}{p_x}\right\} \qquad \textit{back azimuth} \tag{2.1.6}$$

From figure 2.1.3, it is clear that the different arrays show a totally different response for vertically incident plane waves at different frequencies. One can state therefore, that a particular array has an optimal bandwith in which infrasonic events are correctly detected. The lower frequency bound is dependent on the aperture of the array; the larger the aperture, the lower the low frequency bound. For example, figure 2.1.3 shows that DIA is able to resolve whereabouts of infrasonic events down to frequencies of 0.1 Hz adequately, while it is to be expected that the response peak will be broad for this frequency at DBN and EXL. By experience, one learns that the lower frequency bound is at 0.5 Hz for these arrays, considering the peakness of the main lobe. The arrays, and especially DBN, are not able to assign adequate slownesses to infrasonic events with much lower frequencies.

The upper bound of 20 Hz is because of the instrument sampling rate of 40 Hz. According to the Nyquist-Shannon sampling theorem, aliasing is avoided if the maximum

frequency of the signal being processed is less than half the sampling frequency. In practice, an upper bound of 19 Hz is used in the infrasonic data processing in order to avoid aliasing. To conclude, it is important to apply a proper band-pass filter to the raw data. All arrays are able to deal with frequencies in the infrasonic frequency band.

Although theoretically DIA is able to resolve infrasonic signals with frequencies up to 20 Hz, in practice these signals may get attenuated while travelling over the infrasound array and therefore remain undetected. This is because the detection algorithm is based on a coherency analysis, as will be described in the next section.

Moreover, figure 2.1.3 points out that there is a trade-off between the slowness domain and the existence of (higher-amplitude) sidelobes in the array response, again depending on the array design. The larger the slowness band, the more sidelobes occur in the infrasonic slowness domain. It is therefore of importance to reduce the slowness band to slownesses of interest.

In conclusion, in order to detect infrasonic events adequately, it is important to have a correct array lay-out and to consider the correct bandwith that can be used in the processing at a specific array. This section has shown that the infrasound arrays respond well to vertically incident waves. For unknown events, though, a detection algorithm is necessary to identify the infrasonic source (uniquely). The next section will deal with the detection algorithm itself, which is based upon a statistical measure of coherence of the waveform over all array elements.

2.1.3 Fisher processing and processing parameters

In this section, the Fisher detection algorithm is described, which is used to identify the infrasonic source. The algorithm is based upon a statistical measure of coherence of several input time-series, as proposed by R.A. Fisher; see *Fisher* (1948). In this case, the input time-series correspond to the waveforms on the different array elements. The slowness vector, corresponding to the event back azimuth and apparent velocity, is an important variable in this process and the algorithm tries to find the optimal slowness $\bar{p}$, aligning all waveforms forming a *bestbeam*. The process is comparable to stacking in seismic data processing. As is known from stacking seismic data for random incoherent noise, signal-to-noise ratio improves with a factor $\sqrt{n}$ after stacking n times, because signal adds constructively and noise adds destructively. In *Melton and Bailey* (1957) and *Smart and Flinn* (1971), the detection algorithm is described in time- and frequency-domain respectively. Both approaches will be described here.

Time-domain (TD) Fisher

In time-domain, the Fisher detector is rooted on the ratio F of the signal variance over the noise variance, $F = \frac{\sigma_s^2}{\sigma_n^2}$. The subscripts s and n refer to *signal* and *noise*, respectively. Variance σ^2 is given as:

$$\sigma^2 = \frac{\sum_{i=1}^{n}(x_i - \bar{x})^2}{n-1} \tag{2.1.7}$$

The variance represents the summation of the squared differences from the mean for every sample x_i, divided by the degrees of freedom. The success of the Fisher detector lies with the constructive stacking of signal and inconstructive stacking of noise. After stacking, the noise will exhibit a small variance, while the signal will have a relatively large variance instead. For the slowness for which this Fisher ratio is largest (i.e. where the signal has maximum variance compared to noise), the bestbeam is formed. One is able to set a minimum threshold for the Fisher ratio in order to avoid false detections. The next step in describing the detection algorithm is the description of the noise and signal variances:

The variance of the 'stacked' noise at a time t is given by equation 2.1.8:

$$\sigma_{nt}^2 = \frac{\sum_{c=1}^{C}(x_{ct} - \bar{x_t})^2}{C-1} \tag{2.1.8}$$

where x_{ct} refers to an array element sample at time t. $\bar{x_t}$ represents the average sample value over all array elements C. If equation 2.1.8 is time-averaged, one obtains equation 2.1.9, giving the noise variance for a time-bin, containing T samples:

$$\sigma_n^2 = \frac{1}{T}\sum_{t=1}^{T}\left[\frac{\sum_{c=1}^{C}(x_{ct} - \bar{x_t})^2}{C-1}\right] \tag{2.1.9}$$

An increase of the noise variance can be due to an increase of the sample spread or noise amplitude increase. Before noise variances are calculated, it is important to remove dc-components from individual array component traces. Dc-components influence the noise variance significantly.

The variance of the 'stacked' signal is given as the variance over the time-bin, using the stacked trace (between square brackets), see equation 2.1.10

$$\sigma_s^2 = \frac{\sum_{t=1}^{T}([\frac{1}{C}\sum_{c=1}^{C} x_{ct}] - \bar{x})^2}{T-1} \tag{2.1.10}$$

where $\bar{x}$ equals the time-averaged stacked trace sample value:

$$\bar{x} = \frac{1}{TC}\sum_{t=1}^{T}\sum_{c=1}^{C} x_{ct} \tag{2.1.11}$$

Combining the equations for noise (equation 2.1.9) and signal (equation 2.1.10) variance, one derives an expression for the Fisher or F-ratio:

$$F = \frac{\sigma_s^2}{\sigma_n^2} = \frac{T(C-1)\sum_{t=1}^{T}([\frac{1}{C}\sum_{c=1}^{C} x_{ct}] - \bar{x})^2}{(T-1)\sum_{t=1}^{T}\sum_{c=1}^{C}(x_{ct} - \bar{x_t})^2} \tag{2.1.12}$$

Equation 2.1.12 equals the derivation obtained in *Melton and Bailey* (1957). It can be shown that this Fisher ratio is proportional to the *signal-to-noise power ratio*, as:

$$S/Npower = \frac{1}{C}(F-1) \tag{2.1.13}$$

In equation 2.1.13, F refers to the Fisher ratio, as derived in equation 2.1.12.

Frequency domain (FD) Fisher

Frequency domain Fisher detection is a powerful technique, since propagating wave components are easily recognized and separated from each other. Like in time-domain, the algorithm is searching the infrasonic slowness grid. However, the detection is now based upon a defined power-function, equation 2.1.14.

$$F(\omega,\bar{p}) = \frac{E(\omega,\bar{p})}{E(\omega)-E(\omega,\bar{p})}(C-1) \tag{2.1.14}$$

with:

$$E(\omega,\bar{p}) = \left|\frac{1}{C}\sum_{j=1}^{C} A_j(\omega)e^{-i\omega\bar{p}\cdot\bar{r_j}}\right|^2 \tag{2.1.15}$$

and:

$$E(\omega) = \frac{1}{C}\left|\sum_{j=1}^{C} A_j(\omega)\right|^2 \tag{2.1.16}$$

In equation 2.1.14, $F(\omega,\bar{p})$ refers to the Fisher ratio in frequency domain and $A_j(\omega)$ refers to the amplitude spectrum of the Fourier transformed time-series in equations 2.1.15 and 2.1.16. In equation 2.1.15, the amplitude spectrum is shifted with $\bar{p}\cdot\bar{r_j}$. Subsequently, the normalized energy E is calculated by taking the square of the shifted amplitude spectrum, summed and normalized over the number of array elements C. Thereby the energy of the signal at a point in $f-k$ space is calculated. In equation 2.1.16, the total energy of the signal is calculated.

Essentialy, the power-function in equation 2.1.14 compares for a given frequency value the total energy of the signal with the shifted energy of the signal. Again, the slowness vector corresponding to the maximum Fisher ratio calculated is taken for the event. The factor $(C-1)$ 'de-normalizes' the obtained Fisher ratio, since all energy measures were normalized over the number of array elements. By evaluating the algorithm, information on the coherence of the frequency content of the signal is obtained. An event can subsequently be analysed on basis of its spectral content.

The advantage of frequency domain detection is the detail of the algorithm: in frequency domain, the detector analyzes the signal frequency-by-frequency. This gives insight in what the dominant spectral elements of the detected signal are.

Furthermore, since the Fisher detector is now expressed in terms of energy, it is possible to refine the detection threshold. Recall from figure 2.1.3 that in an array response sidelobes occur, next to the main lobe. It is important in array design that the side-lobes are small and far away from the main lobe, in order to avoid erroneous detections with slowness vectors located in the side lobe. However, because the maximum amplitude of the side-lobes is known, and hence its energy, it is possible to calculate the Fisher threshold above which the beamforming slowness vector must be located in the main lobe.

Important processing parameters and considerations

In infrasound processing, some very important parameters and considerations influence the processing results. These are bandpass filter, time-bin size, Fisher threshold value, slowness grid and considered traces.

As pointed out in section 2.1.2, it is important to consider the frequency band of the signal to be processed in order to get unambiguous detection results. Therefore, before processing, the input signal is bandpass filtered, using a two-way second order Butterworth bandpass filter. The frequency limits are dependent on the considered infrasound array and the phenomenon of interest. For infrasound phenomena, this is usually 1-19 Hz (DBN, EXL). Lower-frequent subsonic events may require lower passbands, as low as current microbarometers allow (0.002 Hz). For all results in this thesis, the passband will be mentioned. Before and after applying the passband, linear trend in the signal is removed. Furthermore, dc-components are removed from the signal to reduce noise variance.

The Fisher detector works through the offered time-series. The time-series are discretized in time-bins. The binsize is defined by N samples. The first bin consist of the first N samples. At which sample value the succeeding bin starts is a processing parameter. For example, the succeeding bin may start at the $\frac{N}{2}th$ sample of the signal. A finer overlap will result in more detailed Fisher processing of the total signal and will therefore take more time. It is important to note that the time-bin is an important processing parameter. If large time-bins are used in Fisher processing, longer-wavelength oscillations are favoured in the coherency analysis in spite of short-wavelength oscillations. After processing is complete, an event list is obtained, consisting of event time, maximum Fisher ratio, apparent velocity, back-azimuth and slowness vector. The event time equals the central point in time of the considered time-bin.

In processing, before a detection is characterized as an event, the Fisher ratio must exceed a predefined ratio threshold value in order to reduce false or too noisy detections. This threshold value is chosen for a specific infrasound array. For DBN and EXL, this threshold equals 7 (SNR power 1), for DIA the threshold equals 3.

Successful alignment of the different array element traces is rooted on the selected slowness grid. For successful infrasound detection, slowness values explaining all possible apparent velocities (speed of sound to infinity) and directions (0°-360°) must be present. However, subsonic events will require a different slowness grid in order to detect the events at their proper velocities (e.g. speed of wind, 20 m/s).

Lastly, it is important to consider traces before processing and delete possible bad traces

from the processing, since these traces tend to lower coherency when applying the signal correlator. Before applying the Fisher correlator, all traces are visually checked on their quality.

2.2 Lightning detection system FLITS

KNMI operates at the moment 4 lightning detection stations in the Netherlands (see figure 2.1.2 and figure 2.2.1) and 3 in Belgium. All stations together form the FLITS network (acronym for Flash Localisation by Interoferometry and Time of Arrival System). One station consist of several antennas. Each FLITS station is equipped with 5 VHF antennas, sensitive around 110 MHz. The VHF array enables event detection and azimuth determination of discharges by means of interferometry. Moreover, every FLITS antenna is equipped with one LF antenna, sensitive around 4 MHz. This sensor enables discrimination between CC and CG discharges and detection of CG discharges. By combining detections at multiple stations, localization of discharges is possible.

The instruments are sensitive to electromagnetic waves in certain (low) frequency bands, since electromagnetic waves are generated during discharges. Especially very lowfrequent radiowaves (ELF, 3-3000 Hz, VLF 3-30 KHz) are generated. However, in practice the antennas seem to be sensitive to other sources as well. In order to minimize the misidentification of a signal as being due to a discharge, the system has to be calibrated. Calibration can take place by validating the discharge detection system with other detection mechanisms, as weather radar (see *Noteboom* (2006)) or infrasound.

The system exhibits two different algorithms to detect, localize and differentiate observed lightning discharges. In the *Direction finding* or DF mode, both CC and CG discharges are localized using interferometry and a triangularization algorithm. Analogous to the infrasound array detections, the measured phase-lags measured at 5 antenna's correspond to direction of discharges. The combination of observations at multiple stations lead to localization. Discrimination between CC and CG discharge occurs by inspection of the LF pulse. Discharges are classified as CG discharges if measured rise- and decay time of the pulse is within a predefined limit at a predefined number of stations (typically 3 or 4). Decay-time is most important, since CG have a relative long decay-time.

However, in the *Time-of-Arrival* or TOA mode, VHF interferometry is used to detect and localize CC discharges only. CG discharge detection and localization is based on the time stamps of signals peaks at LF sensors. By applying an hyperbolic intersection algorithm, CG discharges are localized. For the localization to be unambiguous, a minimum of 4 detection stations must have detected the CG discharge. Thus, the essential difference between DF and TOA detection algorithms is that the former exploits the whole discharge signal (waveform), while the latter uses the time-of-arrival of the discharge signal only. The TOA mode appears to provide more accurate localization results compared to DF, as is concluded from earlier studies.

The central processor gathers event information from all lightning detection stations, including azimuth, time of detection, peak value and time of the signal, rise and decay

time. The final result is an HDF5-archive for one day, containing information on the several discharges. Every line includes time and date of discharge, latitude, longitude, current (0 in case of CC), type of discharge, rise- and decay-time and error of detection. For this study, the temporal and spatial information on the discharges were used. Consider *Holleman et al.* (2006); *Holleman* (2005); *Noteboom* (2006) for detail information on FLITS instrumentation.

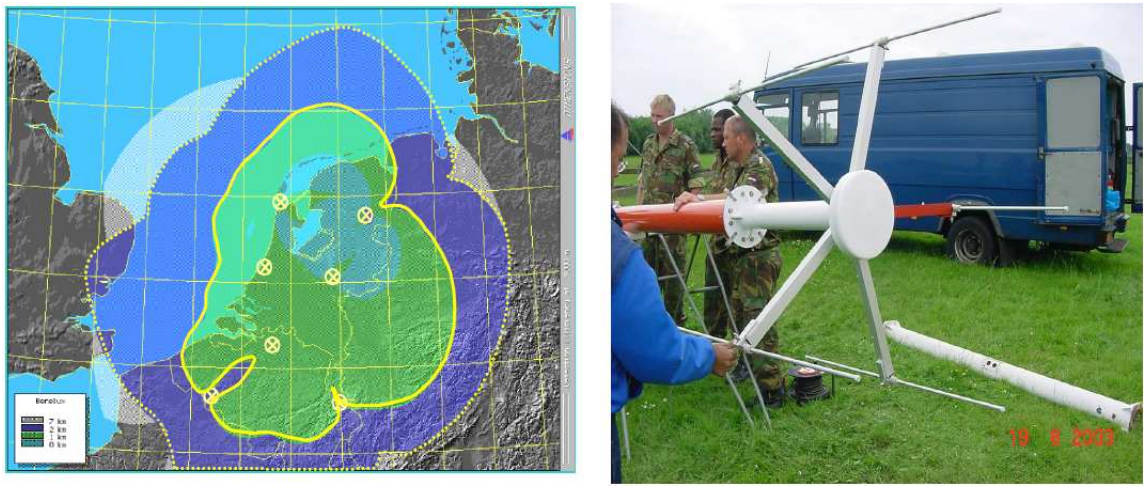

Figure 2.2.1: The left picture shows the location of all FLITS stations in the Netherlands and Belgium. A total of 7 stations forms the detection network. The radius of action of the network is given by the coloured contours. To the right, a FLITS station is shown. The small antennas on top are the VHF sensors, the large white circular sensor in the center is the LF antenna.

Chapter 3

Observations

This chapter describes the processing of infrasound data for case study day October 1, 2006. During this day, a severe thunderstorm moved over a large part of the Netherlands, including De Bilt (DBN) and Exloo (EXL), locations of KNMI infrasound arrays. Consider figure 3.0.1 for a geographic map of CC and CG detections by the KNMI FLITS system. This chapter describes the comparison of the observations from the FLITS lightning detection system and the infrasound array detections. For a detailed description of the detection method and the analysis results, one is referred to chapter 2.

3.1 DBN Infrasound and FLITS observations on 1 October 2006

The FLITS detection and infrasound analysis results are given in figure 3.1.1 for the whole day. A detail figure of timespan 13:00-15:00 UTC is given as well (see figures 3.1.2 and 3.1.3). This particular timespan is of importance since the thunderstorm moved over array DBN. This is clearly observed in figure 3.1.1d, in which the distance of CC/CG discharges from infrasound array DBN is plotted as function of time.

Before continuing to timespan 13:00-15:00 UTC, the processing results of the whole day will be discussed as given in figure 3.1.1. Infrasound detections in figures (b)-(d) are obtained using the Fisher detector, both in time- and frequency domain. Figure (a) is obtained by applying afrequency domain Fisher detector to the waveform data. Hereby, a time-frequency Fisher contourplot is obtained. In processing the DBN data, the time-series are filtered using a 1-19 Hz second order bandpass filter and a binsize of 64 samples is used. Subsequent bins have an overlap of 32 samples. No Fisher ratio minimum is set. The apparent maximum of 7000 m/s in the apparent velocity figure (b) are due to discretizations of the slowness grid: the grid does not allow to resolve even higher velocities. All traces are used in processing the infrasound data. Figures (a)-(e) are very suitable to get insight in the relation between detections of lightning by the lightning detection network FLITS and measured infrasound that day.

In figures (d) and (e), CG discharges are plotted with large green dots, while CC

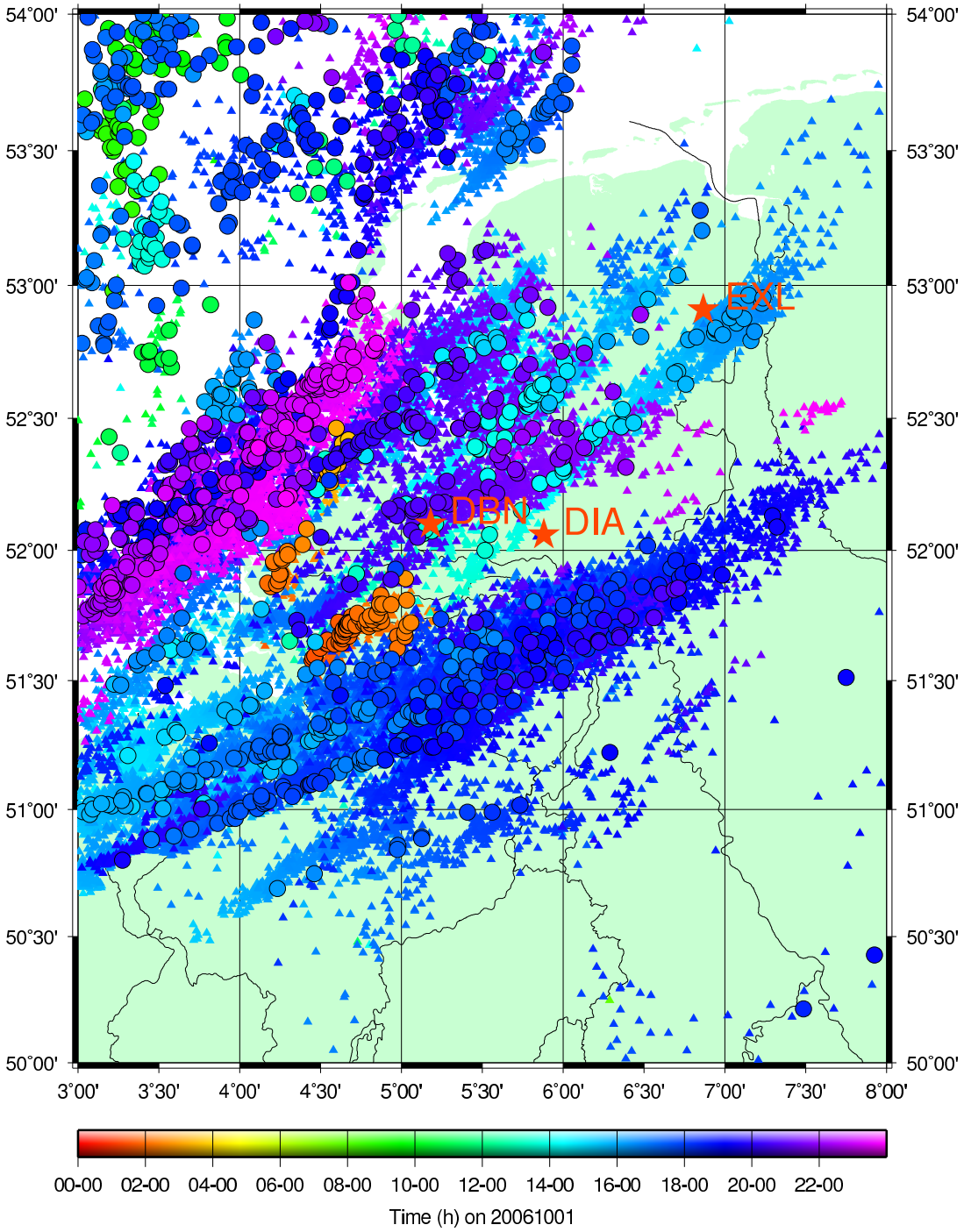

Figure 3.0.1: All discharges as measured by the FLITS detection system at October 1, 2006. Triangles represent CC discharges, circles represent CG discharges. The discharges are color-coded, according to the accompanying timescale. The locations of the used infrasound arrays are given with red stars.

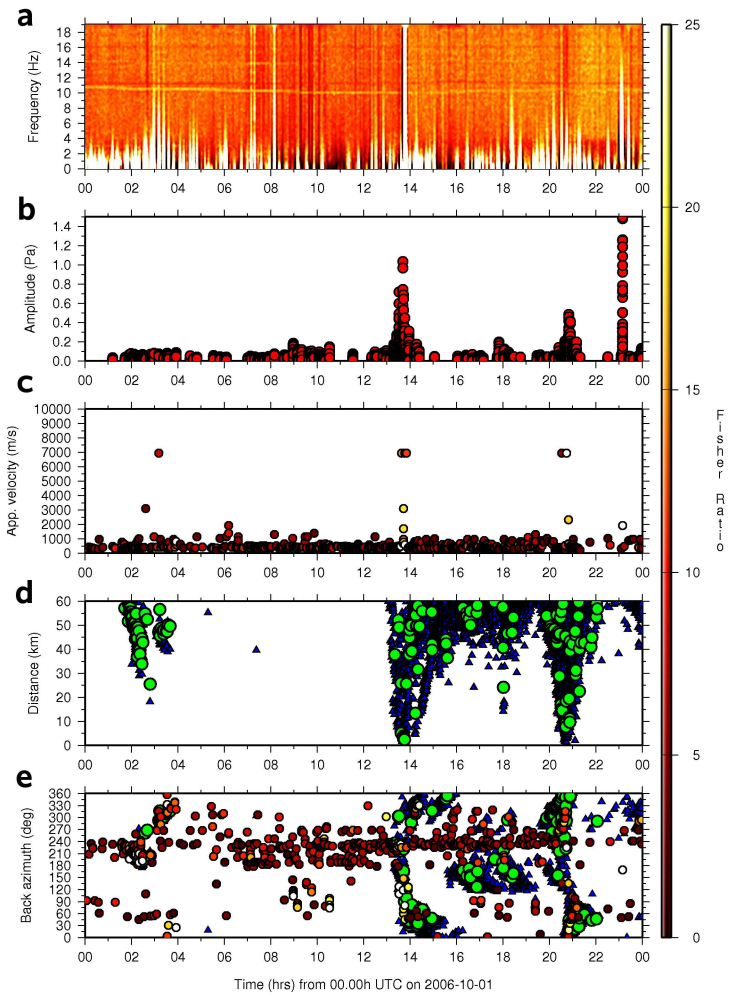

Figure 3.1.1: Infrasound time-analysis results for the DBN array, located in de Bilt, The Netherlands for 1 October 2006. **(a)** Represent a time-frequency power spectrum of the signal and shows the Fisher values for a certain frequency. Lighter colors correspond to higher coherency values (see also the scale on the right of the figure). **(b)** Shows the bestbeam (aligned) amplitude values of the infrasound detections. **(c)** Shows the apparent velocity values of the infrasound detections. The higher the apparent velocity is, the more the wave is vertically incident on the infrasound array. The colors of the separate dots correspond to the Fisher coherency value of the detection. In **(d)**, detected discharges are plotted as distance from the DBN infrasound array. Blue triangles correspond to CC discharges, while larger green dots correspond to CG discharges. **(e)** shows a comparison between infrasound detections and FLITS lightning detection system, both represented with their back azimuth from DBN infrasound array. Blue triangles correspond to CC discharges, green dots to CG discharges. The small dots correspond to infrasound detections; the coloring scale correspond to the Fisher coherency value, similar as in figure **(a)**: lighter colors correspond to higher coherency values.

discharges are plotted with blue triangles. Only CC/CG discharges at distances less or equal than 60 km from DBN are plotted. Infrasound detections are plotted with small coloured dots. The colour of the dots corresponds to the Fisher ratio scale to the right of figure 3.1.1 and thus coherency of the detected signal. Figure (d) shows distance of CC/CG discharges from DBN as function of time. For this day, most discharges in the vicinity of DBN are found in timespans 1:00-3:30 and the timespan 13:00-22:00. Between 13:00-15:00 and 20:00-22:00, the thunderstorm travels over the DBN array, as can be observed from figure (d). In between 15:00-21:00, the discharges are located at larger distances (30 km and up) from DBN. Figure (e) shows the back-azimuth of FLITS detections and infrasound detections w.r.t. DBN array as function of time. The discharges in timespan 1:00-3:30 are located in azimuth range 210°-270°, while the discharges in timespans 13:00-15:00 and 20:00-22:00 are scattered around DBN (0°-360° back-azimuth). In the timespan 15:00-20:00, the direction of discharges is somewhat scattered, between 120° and 210° back-azimuth.

Over the whole day, infrasound detections show a dominant detection back-azimuth of 240°. However, the coherency of the detected infrasound events is rather low, so these events are excluded from our interest. In contrast, interesting infrasound detections are observed with relative high coherency values, during the specified thunderstorm timespans. Especially for the timespan 13:00-15:00, high coherency detections follow the azimuthal trend of the thunderstorm. Similar observations are true timespans 1:00-3:30 and 20:00-22:00. On the other hand, for the timespan 15:00-20:00, infrasound detections do not follow the azimuthal trends of the detected lightning discharges, or at least not so well. This illustrates a clear relation between distance of discharge to an infrasound array and (coherency of) infrasound detections.

Figure (c) shows the apparent velocity values for the detected infrasound events. Important observations to be drawn from this figure are that most detections have apparent velocity values, in the range of the velocity of sound. Thus, most detections belong to events horizontally incident on the infrasound arrays. However, in the timespans of nearby discharges, e.g. 13:00-15:00, events with higher apparent velocity values are detected. Furthermore, these higher values are coupled to event detections with high coherency values. The detected high apparent velocity values correlate well in time with nearby detected discharges, as plotted in figure (d). A relationship between distance and high coherent vertical incident infrasound is illustrated hereby.

Figure (b) shows the absolute amplitude value of all bestbeams in Pascal. A clear rise in amplitude is observed in the timespans 13:00-15:00, 20:00-22:00 and around 23:00. The large amplitude values correlate well in time with nearby detected discharges, except for the large amplitude at 23:00.

Figure (a) gives the spectral content of the infrasound waveform in time. The power spectrum is coloured using the Fisher Ratio coherency scale; therefore, it is observed that most coherent energy is present in the lower frequency band 0-10 Hz. High coherent energy correlates well in time with nearby detected discharges. Especially for the timespan 13:00-15:00, high coherent signal is present over the whole frequency band 0-20 Hz. For timespans 1:00-3:30 and 20:00-22:00, energy becomes less coherent for higher frequencies.

This is consistent with acoustic attenuation theory. Other spectral peaks present in the spectrum do not correlate with discharge detections.

Thus, one may conclude from figure 3.1.1 that there is a strong correlation between spectral coherency, amplitude, apparent velocity and distance of the discharge to the infrasound array. The nearer the thunderstorm is to the infrasound array, the broader and more coherent the infrasound (frequency band), the higher the amplitudes and apparent velocity.

The same observations are given in figure 3.1.2a for timespan 13:00-15:00. From this figure, the relation between amplitude, apparent velocity, spectral coherency peak and distance to the infrasound array is clearly illustrated again. Moreover, it is observed that high coherent infrasound follows the azimuthal trend of the thunderstorm, especially for 0°-240° back-azimuths between 13:00-14:00. For 240°-360° back-azimuths, high coherent infrasound is detected, but later in time, around 16:15. Low coherent infrasound observed at a constant back-azimuth of 240°, as pointed out earlier.

Figure 3.1.2b shows infrasound and FLITS detections in a polar plot. A maximum distance of $r = 60$ km from DBN is considered for the discharges; in the polar domain (r, θ) the center corresponds to DBN. Detected CC/CG discharges are plotted with triangles and circles, respectively. Infrasound detections are plotted with vectors from the DBN array. All detections are coloured based upon the timescale given. CG circle size is based on the maximum measured electrical current of the CG discharge, as measured by the FLITS system. This current value is taken as magnitude value. Although this figure shows a relation in (near) discharge and infrasound azimuth, it also shows that between 345°-45° back-azimuth, no infrasound detections are present. Most detections are between 210°-240°. The fact that the thunderstorm moves from Southwest to Northeast may be the reason for this; infrasound may be hindered by occuring winds. Lastly, figure 3.1.2b reveals no clear relation in maximum electrical current and infrasound detection. Note several nearby CG events not detected by the infrasound array, especially at 300° back-azimuth.

Figure 3.1.3 gives a spatial insight in the relation between lightning discharges as detected by FLITS and infrasound detections. Infrasound event detections are plotted with their respective measured back-azimuths as vectors drawn from infrasound array DBN. A Fisher treshold of $F > 7$ is taken to 'clean up' the image from noisy, low-coherent detections at 210° back-azimuth. FLITS CC/CG detections are plotted with triangles and circles, respectively. All detections are coloured based upon time of detection; figure (b) zooms in on figure (a). The figures show that the DBN infrasound array is especially successful in measuring the direction of nearby CG discharges, as detected by FLITS. However, the concentration of infrasound detections (14:30-15:00) in the 210°-240° back-azimuth range seems to relate very well in time and direction with FLITS detections in Northwest-Belgium. Again, the fact that the thunderstorm moves in the Northeastern direction may be the reason for the abundancy (210°-240°) and lack (340°-40°) of infrasound detections. However, relating FLITS detections one-to-one to infrasound detections does not appear to be possible at large distances. In the Discussion chapter, the association between infrasound, discharge detections and the relation distance to the infrasound array will be

described more thoroughly.

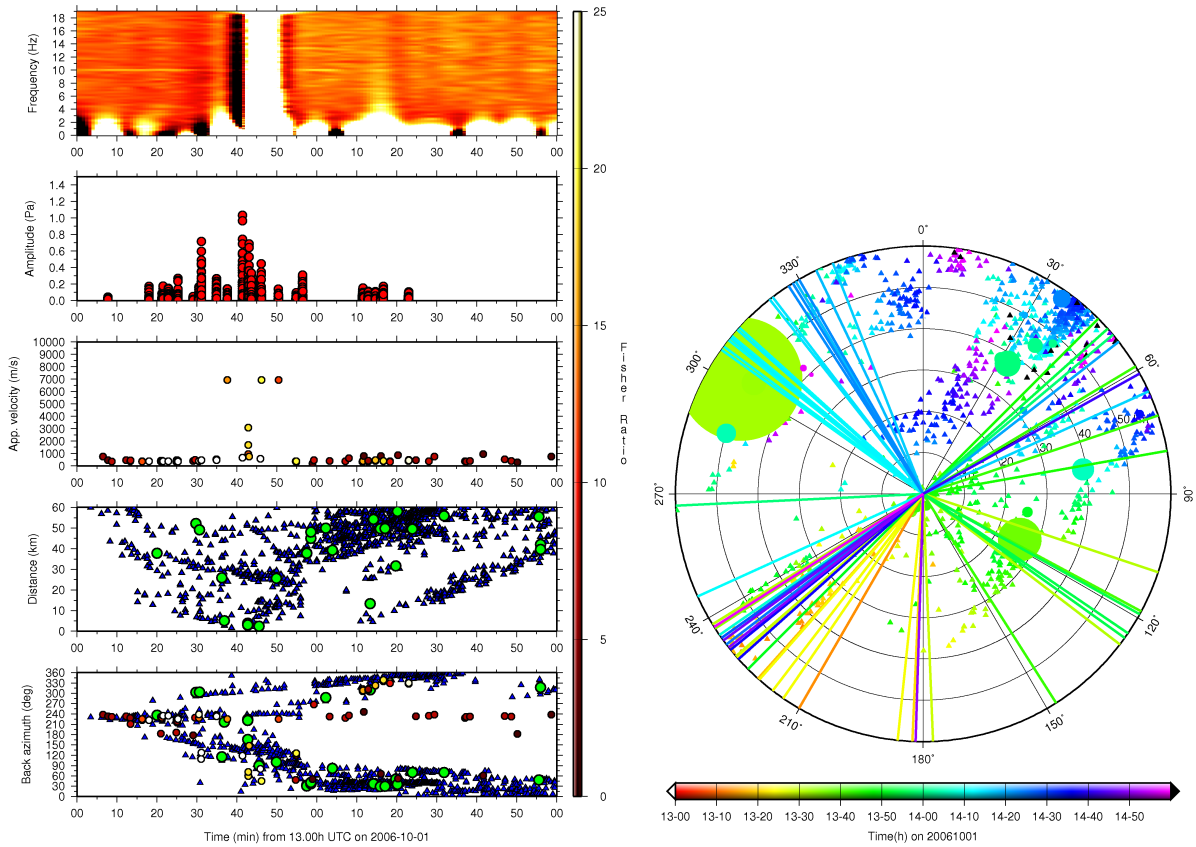

(a) Infrasound analysis

(b) Detections in polar plot

Figure 3.1.2: Infrasound analaysis at DBN on 2006-10-01, for timespan 13:00-15:00 UTC; **(a)** zooms in on figure 3.1.1, **(b)** shows infrasound detections and FLITS discharge detections in a polar plot. Triangles correspond to CC discharges, circles to CG discharges. In **(b)**, the circles and triangles are coloured based upon the given timescale. Moreover, the circles are scaled according to their relative charge. The largest circle at 300°corresponds to 151610 A.

3.1.1 Waveform observations at DBN

Figure 3.1.4 shows infrasonic waveforms measured at the DBN infrasound array elements for several timespans between 13:00-15:00 UTC. Within this timespan, the thunderstorm moved closely over the array. Figure 3.1.4a shows raw unfiltered data. Acoustic events are present within the orange box. Closely after the orange box, a thunderstorm 'nose' is observed; a subsonic pressure disturbance, generated by the thunderstorm front; consider *Wessels* (1964) for a detailed description. The waveform in the orange box of figure 3.1.4a is given in figure 3.1.4b, after applying a bandpass filter (1-19 Hz). Several high coherent

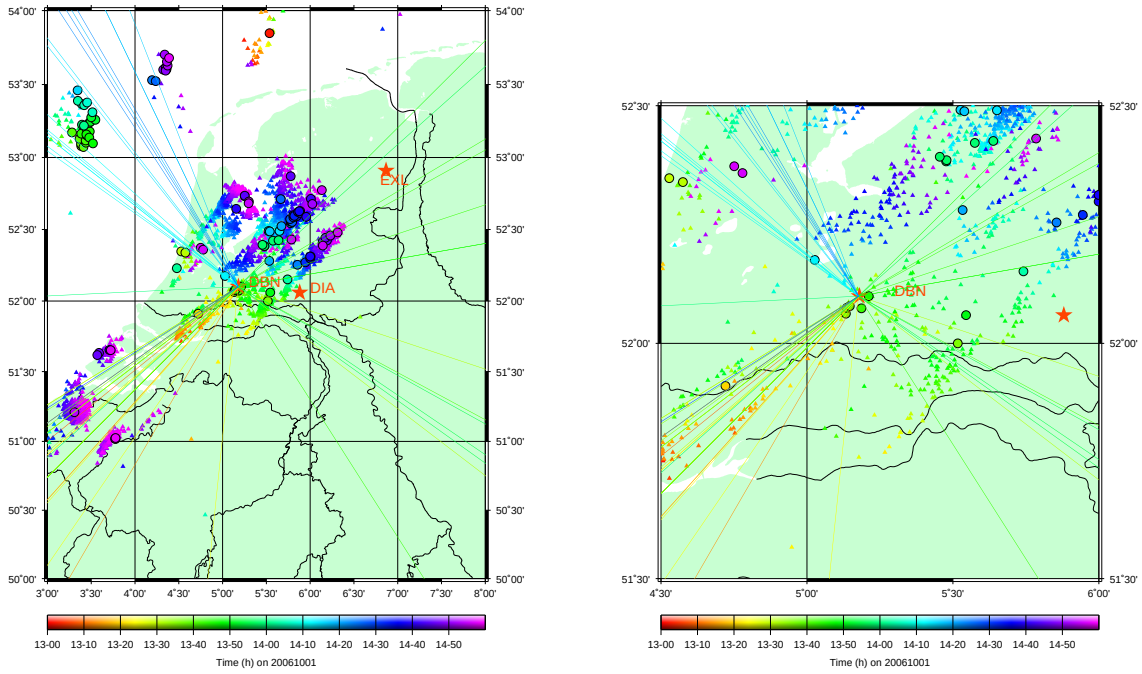

(a) Overview The Netherlands

(b) Zoom-in around DBN array

Figure 3.1.3: Geographical projection of detections by the FLITS system (triangles and circles) and DBN infrasound array (lines from DBN) on 2006-10-01, for timespan 13:00-15:00 UTC. Detections are color-coded based upon the accompanying timescale. Only detections with Fisher Ratio > 7 are shown in order to eliminate the noisy detections at 210° back-azimuth. Figure **(b)** zooms in on figure **(a)**.

infrasonic events can be distinguished in the waveforms. The first set of events is given with more detail in figure 3.1.4c. The first event at 468s cannot be distinguished as an acoustic event because of lack of traveltime differences over the array elements and differing polarity over the array elements. More likely, the signal is explained in terms of electrical discharge on the instruments. From 470s onwards, 6 major coherent infrasonic events can be distinguished. Travel-time differences are observed for these events. These events are in time well correlated with the nearby FLITS CG discharge detections, as presented in figure 3.1.2. The dominant frequency appears to be around 2 Hz, although higher frequencies are present in the waveform as well.

Most waveforms show the general form of a blast-wave: an initial sharp increase of pressure, followed by a sharp drop. Hereafter, the blast-wave returns to equilibrium. Possibly, a so-called 'overshoot' occurs after the drop, before returning to equilibrium.

3.2 EXL Infrasound and FLITS observations on 1 October 2006

Similar infrasound observations are carried out at EXL infrasound array for 1 October 2006. The infrasound analysis results are given in figures 3.2.1, 3.2.2 and 3.2.3. The processing parameters are equal to the processing parameters for DBN. Special attention is given to the timespan 14:00-18:00 UTC. In this timespan, the thunderstorm moved over EXL, comparable to the movement over DBN, as discussed in the last section. In comparison to DBN, the amount of detected infrasound events is much higher, though most are of low coherency.

Figure 3.2.1 shows the combined infrasound/FLITS analysis. The left plot is the analysis for the whole day, the right plot zooms in on timespan 14:00-18:00 UTC. Considering back-azimuths of FLITS detections and infrasound from EXL, high coherent infrasound is observed from the direction of FLITS detections. The coherency of infrasound detections increases with decreasing distance of FLITS detections to EXL. In comparison to DBN, no remarkable high apparent velocity values are found for nearby discharges, apparent velocity values are in the range of sonic velocities. With decreasing distance of discharges to EXL, the amplitude values of the infrasonic bestbeam increase, as observed at DBN. Spectral peaks over the whole infrasonic frequency band are observed for nearby discharges. Moreover, very coherent signal in the >0-5 Hz band appears to be present between 16:00-20:00 UTC and correlates well in time with the passing thunderstorm. Around 22:00, discharges are detected by FLITS. Although the storm appears to be further away, coherent infrasound is detected with relative large bestbeam amplitudes from the same direction. In the spectral domain, coherent energy is observed over the whole infrasonic frequency band. Overall, the coherency of the spectrum is higher than for DBN and more events are detected.

Figure 3.2.2 shows the combined infrasound and FLITS detections in a geographical projection. A Fisher treshold of $F > 7$ is taken to 'clean up' the image. This selection is

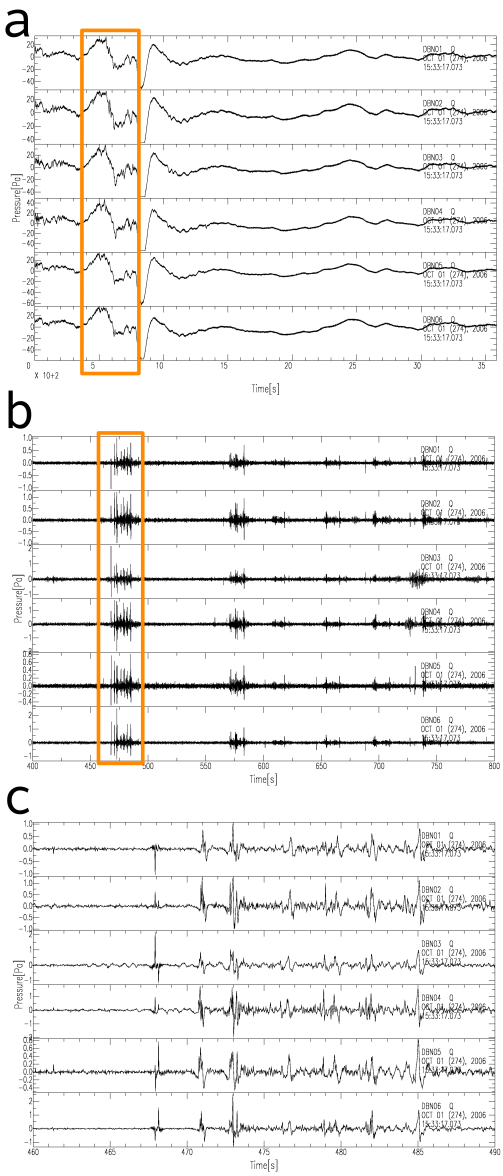

Figure 3.1.4: Infrasonic waveforms measured on DBN infrasound array on 2006-10-01. **(a)** Raw, unfiltered data; timespan 13:33:17-14:33:17 UTC. **(b)** Bandpass filtered [1-19 Hz] waveforms for timespan 13:40:00-13:46:40 UTC. **(c)** Bandpass filtered [1-19 Hz] waveforms for timespan 13:41:00-13:42:30 UTC. Figure **(b)** zooms in on **(a)**, figure **(c)** on **(b)**.

not carried out for figures 3.2.1 and 3.2.3. The right figure zooms in on a region in the vicinity of EXL. The figures show the good agreement of FLITS detections and infrasound detections in space and time, especially within the orange box. Some infrasound detections may even be associated with events at large distances (out of the orange box). However, ambiguity can play a role; consider for example the NW detections in the timespan 17:40-18:00 which can associated to nearby and far away discharges. It is more likely, though, that the detections are related to nearby discharges. Multiple array detections probably lead to more conclusive associations. In section 3.3 this will be further discussed.

The infrasound and FLITS observations are given in a polar plot in figure 3.2.3. The agreement in bearing and time is again observed here. However, it is noticable that some nearby (30 km) CG discharges are not detected by the infrasound array, for example around 15:40 at 200° back-azimuth.

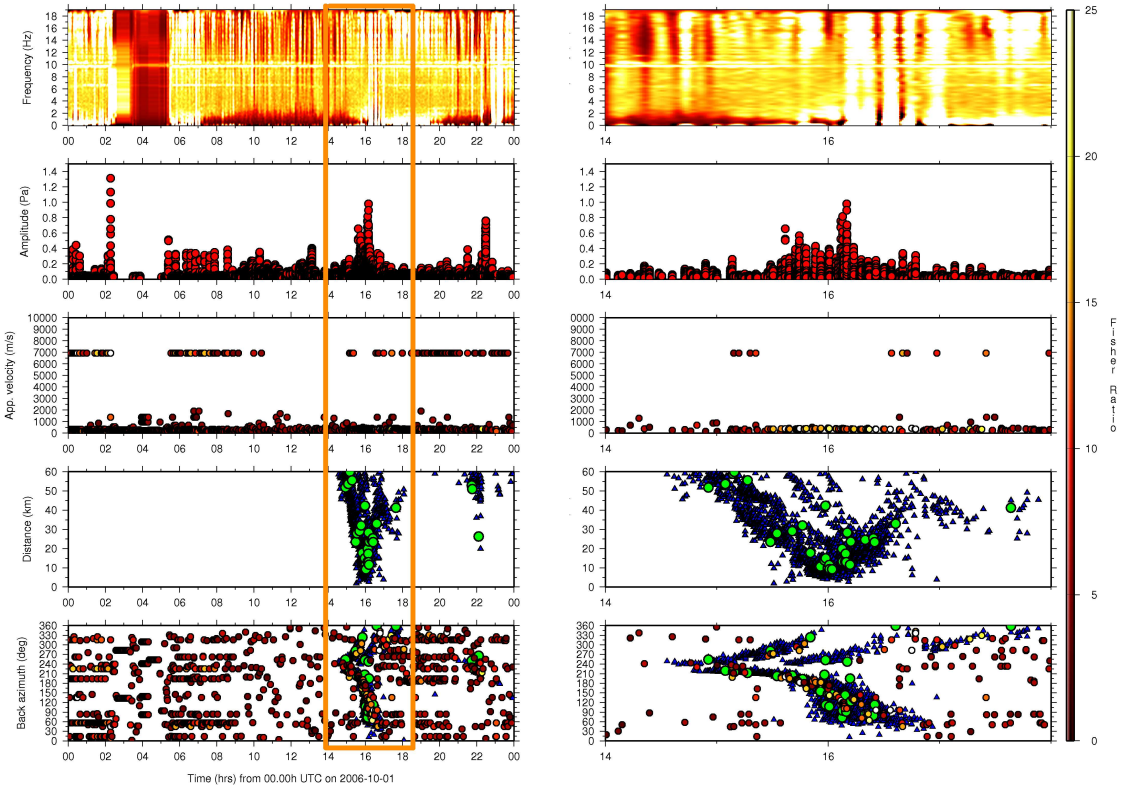

Figure 3.2.1: Infrasound analysis at EXL infrasound array for 2006-10-01. The left figure shows the analysis for the whole day, the right figure zooms in on timespan 14:00-18:00 UTC; for a discription of the results, consider the text.

3.2.1 Waveform observations at EXL

Similar to the waveform analysis at DBN, EXL waveforms are given in figure 3.2.4. Again, infrasonic energy is observed to precede a thunderstorm nose. Filtered data reveals that

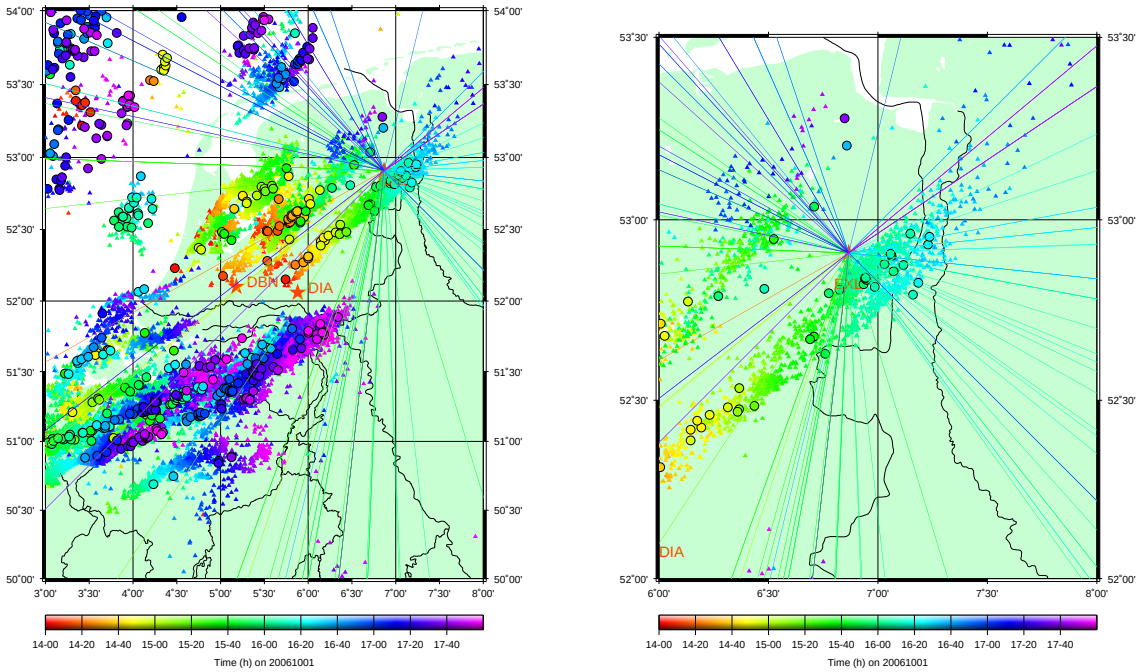

(a) Overview The Netherlands

(b) Zoom-in around EXL array

Figure 3.2.2: Geographical projection of detections by the FLITS system (triangles and circles) and EXL infrasound array (lines from EXL) on 2006-10-01, for timespan 14:00-18:00 UTC. Detections are color-coded based upon the accompanying timescale. Only infrasound detection with Fisher Ratio > 7 are plotted, because of the large number of EXL infrasound detections. Figure **(b)** zooms in on figure **(a)**.

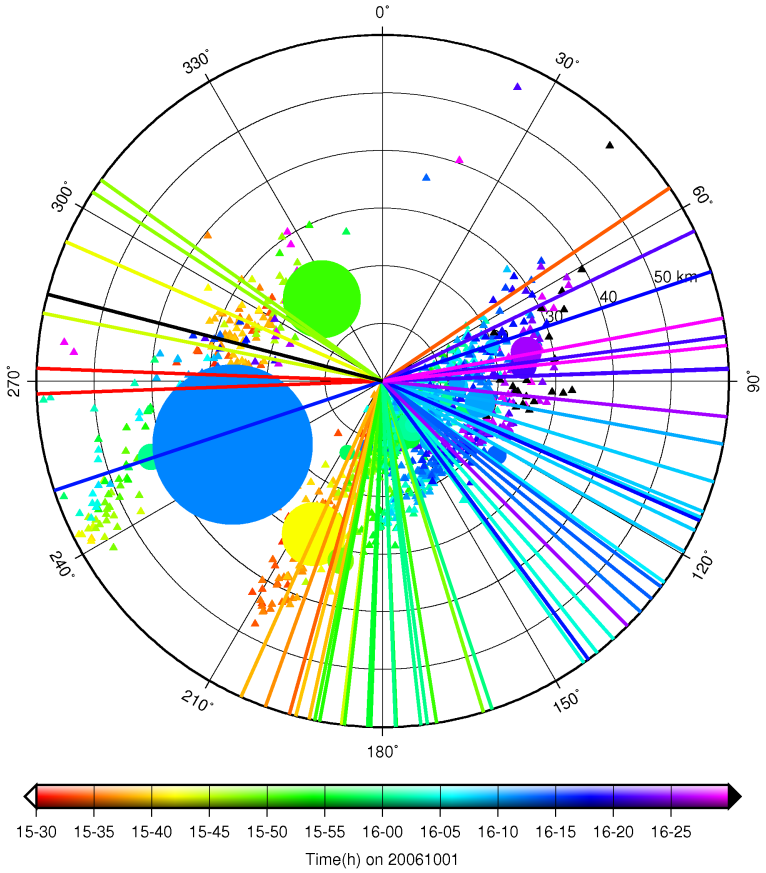

Figure 3.2.3: The figure shows infrasound detections at EXL and FLITS discharge detections in a polar plot. The selected timespan is 15:30-16:30 UTC on 2006-10-01. Triangles correspond to CC discharges, circles to CG discharges. The circles and triangles are coloured based upon the given timescale. Moreover, the circles are scaled according to the maximum measured electrical current. The large circle at apt 240°corresponds to 74400 A.

the associated infrasound has a blast-wave form: an initial increase in pressure, a sharp pressure drop and equilibrium. Overpressure is not so evident in this timespan. The infrasonic events in figure 3.2.4bc are well associated in time with nearby FLITS detections, as presented in figure 3.2.1

3.3 Crossbearing of multiple arrays, DBN and EXL

As discussed in the last sections, single array detections are well correlated in time with thunderstorm discharges. However, single array detections are not able to locate discharges unambiguously. In order to reduce ambiguity on infrasound detection of lightning, multiple arrays can be used. By combining back-azimuths measured at multiple arrays for one event, the location of the source can be estimated. This is called *crossbearing localization*. It was shown in the preceding sections that the FLITS detections correlate well with infrasound detections in time and direction, at least up to 50 km array distance. Therefore, combining the detection abilities of these two infrasound arrays, DBN and EXL, is a logical next step in order to localize a lightning source using crossbearing. For this purpose, all FLITS and infrasound detections are combined in non-overlapping time-bins of 5 minutes for the considered day 1 October 2006. The time-bin size is considered to be appropriate based on theoretical tropospheric direct wave sound propagation.

Unfortunately, crossing array detections are not often in the vicinity of FLITS detections. For timespan 20:40-21:00, the results are given visually in figure 3.3.1. One of the crossbearings actually is in the vicinity of FLITS detections. An analysis of this crossbearing at (5°10',52°45') rejects this crossbearing as a localization of a discharge, since none of the detections at arrays DBN and EXL can explain the thunderstorm activity well at this point in time and space.

Therefore, it is more probable that the infrasound detections are associated to discharges closer to the infrasound arrays or to other sources. In the Discussion chapter, the association between infrasound, discharge detections and the relation distance to the infrasound array will be discussed further.

3.4 Observations on thunderstorm fronts

A typical meteorological phenomenon which can be observed using infrasound arrays are very low-frequent subsonic heavy pressure drops. Because of low propagation velocities, infrasound arrays can detect the whereabouts of these low-frequent events adequately. However, these events are not classified as infrasound due to the low velocities. Pressure drops can be associated with several meteorological phenomena; thunderstorm fronts are typical examples and the associated pressure drops are referred to as thunderstorm 'noses'; condider *Wessels* (1964). Examples of such noses are given in figure 3.1.4 and 3.2.4.

In this section, the observation and propagation of such a nose is described for 28 February 2007. Between 12:00 and 13:00 UTC, heavy pressure drops are observed at DBN

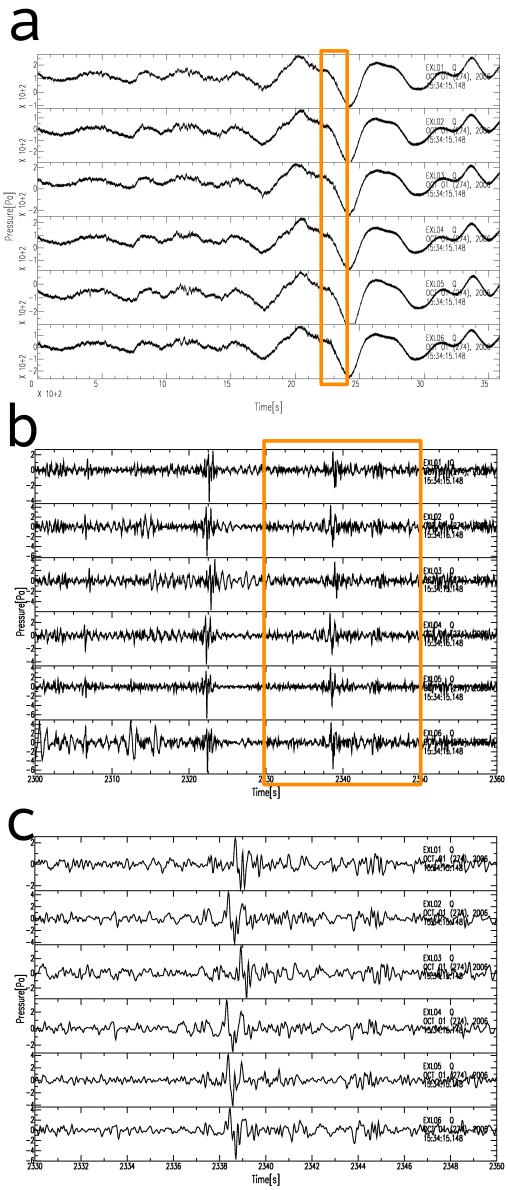

Figure 3.2.4: Infrasonic waveforms measured on EXL infrasound array on 2006-10-01. **(a)** Raw, unfiltered data; timespan 15:34:15-16:34:15 UTC. **(b)** Bandpass filtered [1-19 Hz] waveforms for timespan 16:12:35-16:13:35 UTC. **(c)** Bandpass filtered [1-19 Hz] waveforms for timespan 16:13:05-16:13:25 UTC. Figure **(b)** zooms in on **(a)**, figure **(c)** on **(b)**.

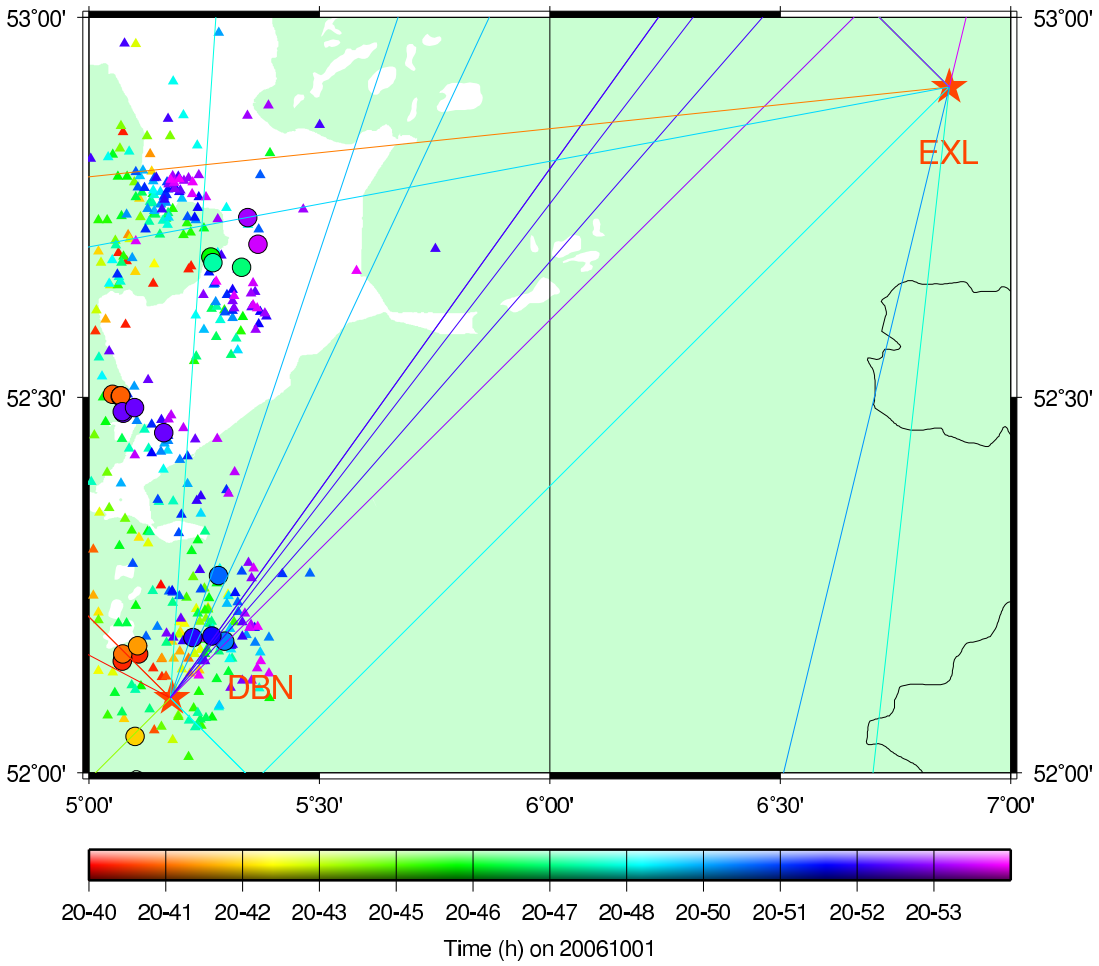

Figure 3.3.1: Crossbearing image for the timespan 20:45-21:00 UTC on 2006-10-01. The image shows an apparent correct crossbearing around 20:49, at 5°10', 52°45'

and DIA infrasound arrays. Because thunderstorm noses are subsonic events, as is evident from the traveltime over an infrasound array, the slowness grid for Fisher processing is adjusted in the detection algorithm. Thunderstorm noses travel more or less horizontally, with the speed of the wind, around 15 m/s. Therefore, the slowness grid is adjusted in order to include subsonic velocities, instead of (usual) sonic velocities. For both arrays, one hour of raw data is lowpass filtered with a corner frequency of 0.05 Hz. A bin is set to contain 8192 samples and subsequent bins have 1024 samples overlap. With a sampling frequency of 40 Hz for the microbarometers, this corresponds to 204.8 s and 25.6 seconds respectively.

Consider figure 3.4.1 for the infrasound analyses at both arrays. The plots show detections of subsonic events for which Fisher Ratio > 7. The upper window shows the pressure variation over time and clearly shows the thunderstorm nose. The thunderstorm nose appears to have a dominant period of 200s and large amplitude values up till 40 Pa. The second window plots for an event detection the maximum Fisher ratio in the consulted segment of time. The velocity and back-azimuth corresponding to the slowness vector/maxiumum Fisher ratio are given in the third and fourth, respectively. It is assumed in interpretation that apparent velocity equals true velocity. At DBN, a very high Fisher ratio of 120 is found at the onset of the thunderstorm nose at 12:10 UTC. Event velocities of 15 m/s are found, in accordance with the meteorological observations; event's back-azimuth is 250°. Observations at DIA are quite similar to DBN. However, one can distinguish two maxima in the Fisher ratio plot. The first Fisher Ratio maximum of 50 is at the onset of the large thunderstorm nose at 12:30 UTC. A second, higher Fisher maximum of 60 is at 12:44 UTC, at the onset of a less expressed, but more coherent, second nose. For DIA, both maxima are coupled to event detections at 250-260°. Event parameters velocity and back-azimuth appear to be less well resolved for the detections at DIA. This might be due to the larger aperture of the infrasound arrays, thereby reducing coherency between array elements. Reduced coherency is indicated by the lower Fisher ratio as well.

The thunderstorm nose detections at DBN and DIA are given in a geographical projection in figure 3.4.2, together with FLITS detections for timespan 12:00-13:00 UTC. The figure shows the WSW-ENE trend of the thunderstorm. Furthermore, it is shown that subsonic pressure disturbances are observed at ca. 240° back-azimuth, around 12:12 at DBN and around 12:31 at DIA. The thunderstorm evolves from the same back-azimuth to 60° azimuth. This indicates that the arrays detect the direction of the thunderstorm and its front, the nose, correctly.

3.5 Lightning discharges and atmospheric attenuation

Mechanical waves are subject to attenuation. Attenuation is generally defined as loss of wave-energy with travelled distance, resulting in a decrease of amplitude. As mentioned in the introduction chapter, infrasonic waves travel over a long range compared to (normal) sonic waves, because the acoustic absorption coefficient is proportional to the square of the frequency. Due to attenuation, a 1 kHz will lose 90% of its energy after 7 km travelling

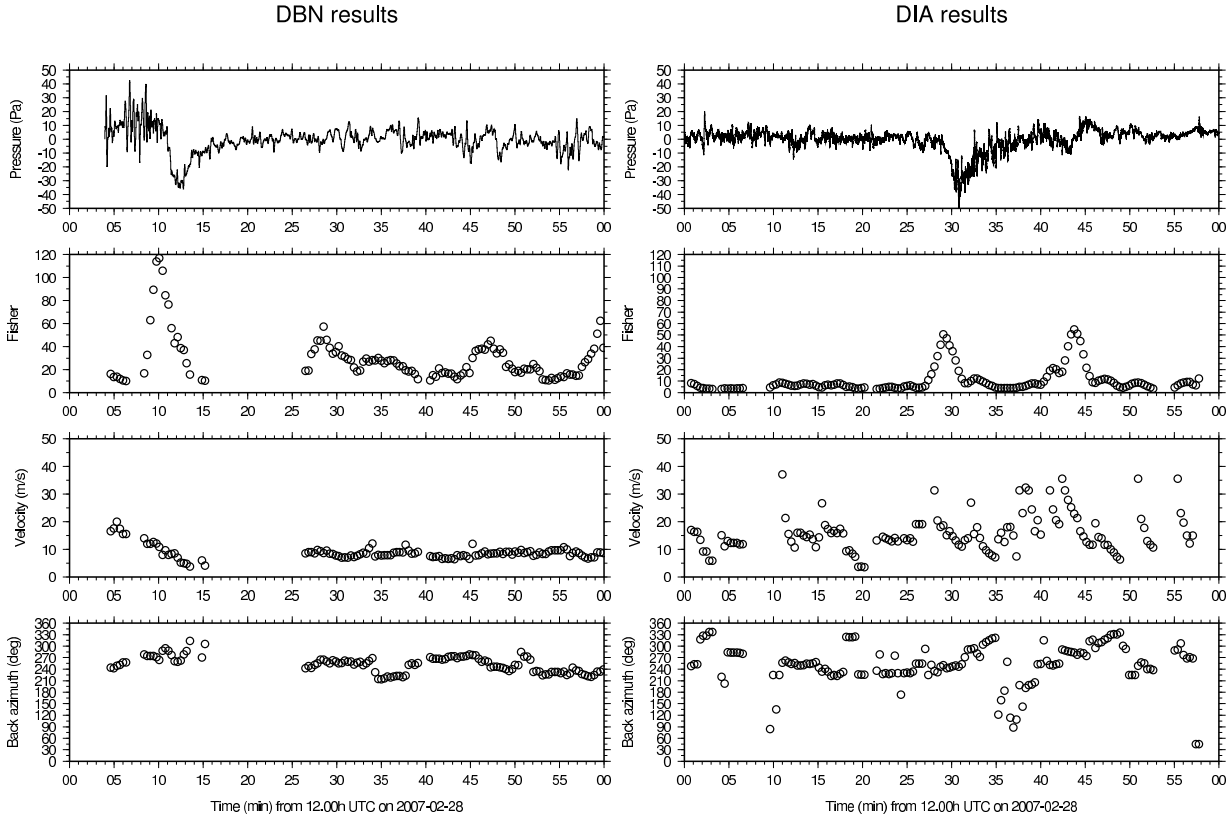

(a) DBN (b) DIA

Figure 3.4.1: Time-domain Fisher processing results for the low-frequent subsonic thunderstorm nose as discussed in this section. Figure 3.1(a) and 3.1(b) give results for processing at DBN and DIA infrasound arrays respectively. The plots show events for which Fisher Ratio > 7.

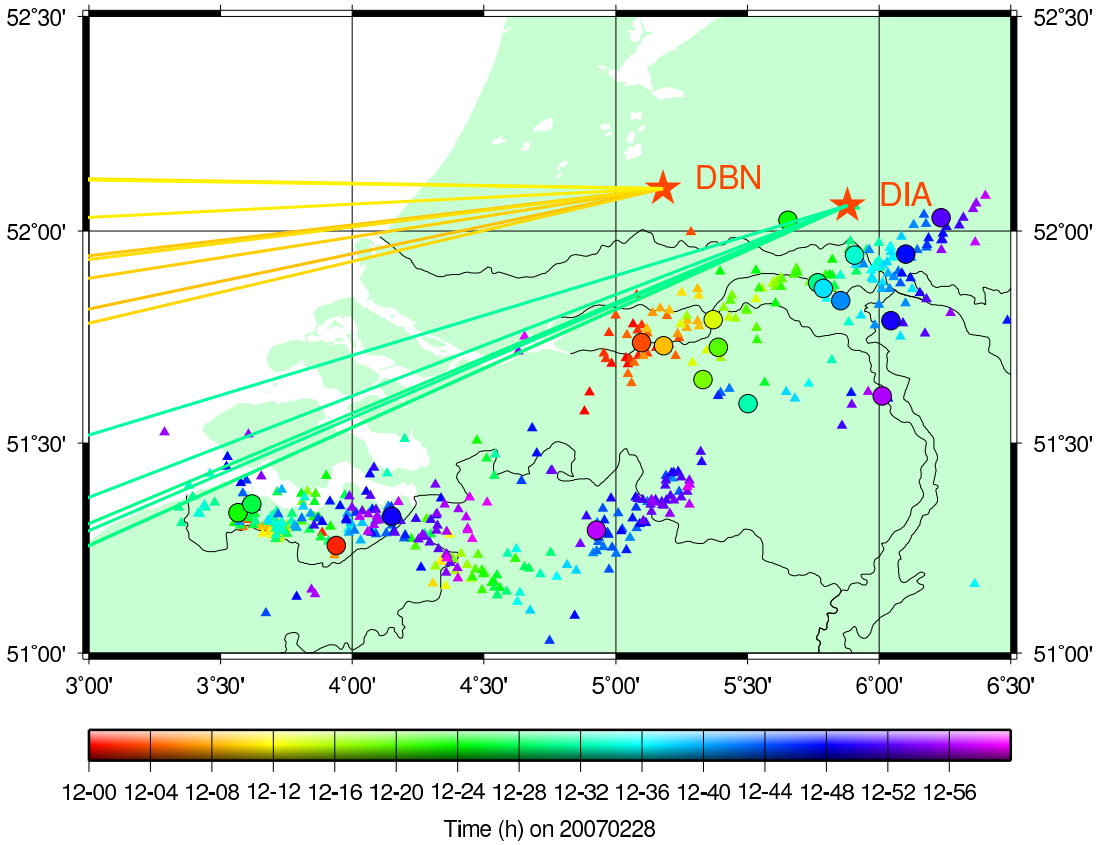

Figure 3.4.2: Geographic projection of FLITS detections and **subsonic** detections on 28 February 2007 during timespan 12:00-13:00 UTC. FLITS CC/CG detections are plotted using triangles and circles, respectively. **Subsonic** detections detections are plotted with vectors drawn from the infrasound array to the observed back-azimuth. FLITS and **subsonic** detections are coloured based on the timescale given. Consider the text for a detailed description.

at sea level, while for a 1 Hz signal this distance equals 3000 km. In order to investigate to which amount the associated infrasound waveform amplitude is sensitive to attenuation mechanisms, amplitude values, picked for associated infrasound, are plotted against distance to the infrasound array.

In order to pick waveforms correctly, five days with closeby thunderstorm activity are selected, in the period 2003-2007. Since CG discharges are more intense sources and probably better detected with infrasound arrays, considering previous sections, the most intense CG discharges are selected for these five days within a range of 20 km of DBN array. Maximum electrical current, rise and decay times is measured with the FLITS measuring system. Different measures can be taken for the intensity of a discharge. Perhaps the best measure is the integrated electrical current over time. However, because of practical reasons, the maximum electrical current is taken as an intensity measure for CG discharges.

For these intense CG discharges, expected infrasound arrivals are calculated with a direct wave tropospheric propagation model. Subsequently, infrasound time series are searched using these expected arrival times, for characteristic lightning waveforms as discussed in preceding sections on waveforms. For associated waveforms, amplitudes are picked and normalized for the corresponding discharge current. Normalization is carried out in order to be able to compare amplitudes of associated waveforms at different distances, as independent as possible from the discharge's intensity. Hereby, a linear relationship between discharge intensity and infrasound amplitude is assumed. The normalized values are multiplied with a factor 1000 and plotted against distance. Results are given in figure 3.5.1.

The results show a decaying trend of the ratio with distance, as expected from theory. The normalized values are plotted with orange dots. Since it can not be inferred uniquely what relation exist between the amplitude of observed infrasound and distance, no empirical relation is drawn in the figure. In the Discussion chapter, the results will be discussed and explained further in terms of attenuation mechanisms.

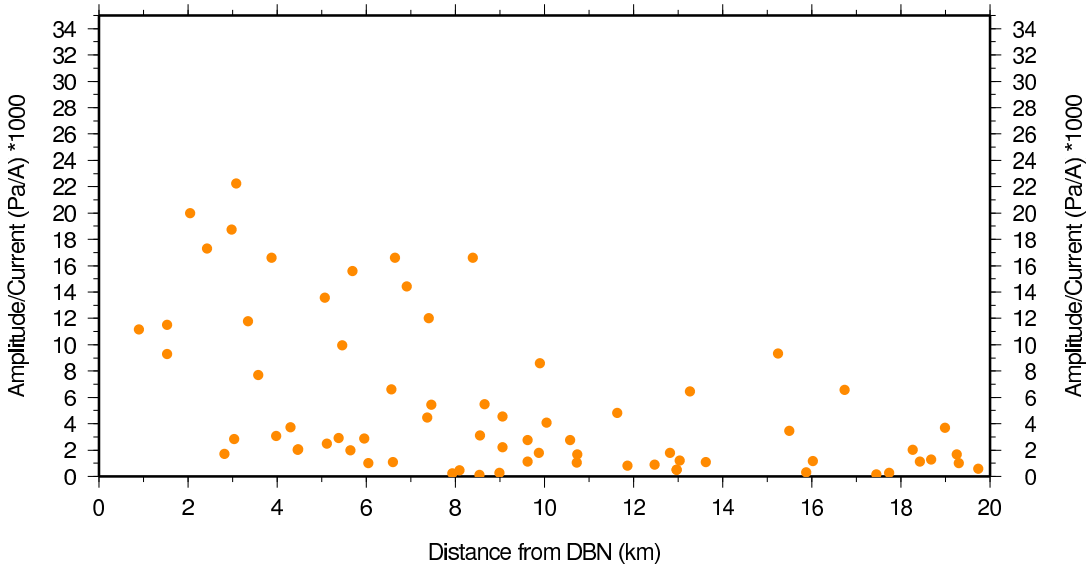

Figure 3.5.1: Attenuation relation for associated infrasound. The orange dots represent the normalized datapoints.

Chapter 4

Discussion

In this chapter, the results will be discussed in terms of the study objectives and associated uncertainties. Therefore, this chapter will address topics on the detectibility of lightning discharges by infrasound, the content and behaviour of associated infrasound. Moreover, by comparing infrasound detections to FLITS detections, it will be discussed whether infrasound is a fruitful verification tool for the FLITS network.

4.1 Detectibility of lightning discharges with infrasound

In section 3.1 and 3.2, infrasound detections and FLITS detections are combined in different plots, giving insight in the relation between acoustic and electromagnetic signals from thunderstorms. In these sections, day 1 October 2006 is chosen because of the spatial distribution of FLITS detections around infrasound arrays DBN and EXL. This enables one to investigate the detectibility of lightning with infrasound, by comparing event detections with both measurement techniques. Later on in this chapter, the comparison and verification of infrasound with FLITS will be further discussed.

4.1.1 Meteorlogical situation & infrasound detections

Figure 3.0.1 shows that the thunderstorm at 1 October 2006 is very severe and that many CC/CG discharges have been detected by the FLITS network. Moreover, it is obvious that strong SW-NE strong winds occur this day, considering the time of detections of the discharges. One should note that suchlike turbulent atmospheric conditions may hinder infrasound propagation or may mask the precise direction of infrasound when the infrasound source (thunderstorm activity) is near.

In figures 3.1.3 and 3.2.2, infrasound detections with Fisher Ratio > 7 for respectively DBN and EXL are given in a geographical projection, together with discharges as detected by the FLITS network. Both figures show that most thunderstorm activity in a radius up to 50 km corresponds well in time and direction with infrasound detections. Especially

CG discharge directions are well resolved by exploiting infrasound. However, not every direction in which the storm is active is detected properly. Especially figure 3.1.3 shows that discharges with back-azimuth 345°-45° w.r.t. the array are not detected. Again, occuring winds may be hindering infrasound propagation; on the other hand, the discharges could be beyond the reach of the DBN infrasound array. Moreover, most of the FLITS detections in this specific area are distinguished as CC discharges. Lowering the Fisher treshold in the maps does not essentially alter the image.

A qualitative relation between meteorlogical conditions (winds) and detectibility of lightning discharges with infrasound is apparent from the current observations. Future studies, incorporating wind profiles may quantify this relation.

Apart from hindering infrasound propagation, wave propagation paths may also deviate because of occuring winds. It is to be expected that the deviation increases with increasing propagation path length. This path length is for direct waves defined as the distance from discharge to the infrasound array. By associating an infrasound detection to a certain discharge, as detected by the FLITS network, the deviation can be calculated by comparing back-azimuths of FLITS and infrasound detections. This implicity assumes that the localization of FLITS has low uncertainty and that the amount of false detections is very low. Further on in this chapter, both datasets will be compared in a statistical way.

4.1.2 Relations between infrasound parameters and lightning discharges

From figures 3.1.1 and 3.1.2 (DBN) and from figure 3.2.1 (EXL), one may conclude for both infrasound arrays that there is a good correlation between occuring CG discharges and high coherent infrasound. If only CC discharges are detected in a time-span, infrasound observations are absent or low coherent. Apparent correct detections of distant CC discharges around 13:10 in figure 3.1.2 are to be rejected since low-coherent energy comes from this direction constantly. Therefore, these detections can be regarded as not of interest.

Furthermore, it is obvious from these figures that infrasound coherency is a function of distance from the infrasound array. Near discharges will be detected more easily, because waves experienced less attenuation. For larger distances, infrasound detections can be associated to FLITS CG detections, but not so well to CC discharges. It can be stated that acoustic signal CC from lightning discharges is hampered to much by the atmosphere to be detected by infrasound arrays at distances larger than 5-10 km.

A relation between apparent velocity of associated infrasound and distance of the FLITS discharge to the array is clearly shown in the figures. Very near discharges (< 5 km) are apparently more vertically incident than more distant discharges. The bestbeam amplitude of infrasound associated to nearby discharges is relatively high. The spectral content of the signal over time reveals that most energy resides in the lower part of the infrasound frequency band, < 10 Hz. The frequency band of coherent infrasound energy increases in the direction of 20 Hz for less distant CG discharges.

4.1.3 Crossbearing studies

In section 3.3, the attempt to use multiple array detections for the purpose of crossbearing localization of lightning discharges is described. In this section, detections at DBN and EXL are combined. Unfortunately, none, or few, of the detections over the day appear to be able to be combined with each other. The presented figure in that section shows that within a certain time-span, crossing event detections appear in the vicinity of thunderstorm activity, but the specific thunderstorm activity as detected by FLITS does not appear to be consistent with the infrasound detections. Probably, the detections are to be associated with thunderstorm activity at smaller distances. Thereby, ambiguity is solved in a way, since nearby FLITS detections can be associated to the infrasound detections better, but this is still a bit unsatisfying.

The reason for the lack of crossbearings could be found in the large distance between DBN and EXL and the lack of overlapping 'radii of action'. As discussed in the preceding section, single infrasound arrays offer good detections of thunderstorm activity in terms of back-azimuth, certainly up to 50 km. Therefore, it can be stated that the radius of action of a single array for thunderstorms is at least 50km. The large distance between DBN and EXL does not allow to combine the detection results and localize events. Meteorlogical conditions (winds) could decrease the radius of action of an infrasound array to a certain back-azimuth.

The inconsistency of thunderstorm activity and infrasound detections could on the other hand be explained by other mechanisms. In coming to the conclusion as stated above, a direct wave tropospheric travelpath is assumed since discharges between clouds and the Earth appear to happen in the troposphere. Deviating paths, i.e. refractions, could enable significant traveltime differences in a layered atmosphere with significant velocity contrasts. However, it appears that the lower 2 km of the atmosphere, i.e. the lower part of the troposphere, is rather homogeneous. Furthermore, activity of winds could be regarded as well. However, significant wind velocity increases appear to be higher in the atmosphere. Lastly, one could argue that discharges have gone unnoticed by the FLITS network. This argument will be dealt with in the last section of this chapter.

In order to test whether arrays with shorter interarray distance are able to do crossbearing localization of lightning discharges, infrasound array DIA (Deelen Airforce base, The Netherlands) is selected as candidate. However, this array is extremely large in comparison to DBN (1500m aperture instead of 70m). Therefore, the array has a different optimal bandwith of infrasound detection, much lower in frequency. DIA has been used intensively, for example to detect low-frequent infrasound from Mt. Etna; see *Evers and Haak* (2003). At 28 February 2007, a thunderstorm moved over the Southern part of The Netherlands, passing DBN and DIA. This day is selected for analysis, consider figure 3.4.2 for a geographical map of the FLITS detections as function of time.

However, by inspecting DIA array element traces, it appears that no coherent energy is present over the array, even for nearby thunderstorm activity. While thunderstorm activity is clearly visible on the traces as a subsonic pressure drop; as discussed in section 3.4, Fisher detection for infrasound events yield no results. This illustrates the inability

of DIA to detect associated infrasound from lightning: the coherency of the events over the array elements is too low. Future studies may possibly enable detection, by exploiting sub-arrays within the 16-element DIA array.

4.1.4 Detection statistics

In order to give a quantitative, statistical representation of the relations between distance of FLITS detected discharges vs. coherency, apparent velocity and deviation of associated infrasound is given in figure 4.1.1, for DBN and EXL. At days with thunderstorm activity, as detected by FLITS, FLITS discharge detections are compared with contemporary infrasound detections. By allowing for a certain deviation in detected back-azimuth and for a certain time-window for infrasound waves, FLITS and infrasound detections are associated. Infrasound detections with apparent velocity values lower than 320 m/s are not considered in the association, because apparent velocity values lower than the speed of sound are physically infeasible. The association is carried out separately for CC and CG discharges in order to discrimate between a relation CC-Infrasound and CG-infrasound.

The allowed time-window is defined between 0 seconds and $t = \frac{d_{flits-dbn}}{v_{sound}}$; for deviation in back-azimuth, -5°$< \Delta\phi <$ 5° is allowed. Infrasound and FLITS detections falling in these categories are correlated with each other. Thereby it is possible to express infrasound parameters as function of discharge distance to the infrasound array. Considered parameters are Fisher ratio, deviation in back-azimuth and apparent velocity.

These statistical relations between infrasound parameters and FLITS discharge detections can be used to discuss the detectibility of lightning discharges with infrasound in a more quantitative point of view. Hereby, one assumes that by relating both datasets, infrasound is associated to FLITS detections correctly. Since the correlation is carried out for the different types of discharges and for DBN and EXL separately, one is able to discuss the differences and similarities between the relations as function of discharge type. Because the two arrays are spatially too distant from each other, 'differences' in the statistical plots between the two arrays are not considered; however it appears sound to compare the general trend in the plots for both arrays. For EXL, less days of thunderstorm activity are used because EXL only provides with real-time data since August 2005.

Consider the plots with the red dots, representing the relationships between Fisher ratio of associated infrasound (measure of S/N power ratio) and distance of the discharge to the infrasound array. As wave-energy decays with distance, the Fisher ratio of associated infrasound should decrease with distance as well. This hypothesis can be tested on the statistical plots. For CG discharges at both arrays, a decrease is observed, up till 70-80 km distance. Beyond this distance, Fisher ratios increase with distance; since it is not very feasible that such high coherent infrasound is associated to distant thunderstorm activity, the extent of the detection is interpreted to be at 70 to 80 km distance. The relation is most clear for the DBN statistics; for EXL the relation is probably poorer because of the low data availability and hence the lower chance of association.

For CC, the relationship is non-existent or at least not clear from these statistics; consider the energetically unfeasible increase in Fisher ratio with distance for the CC as-

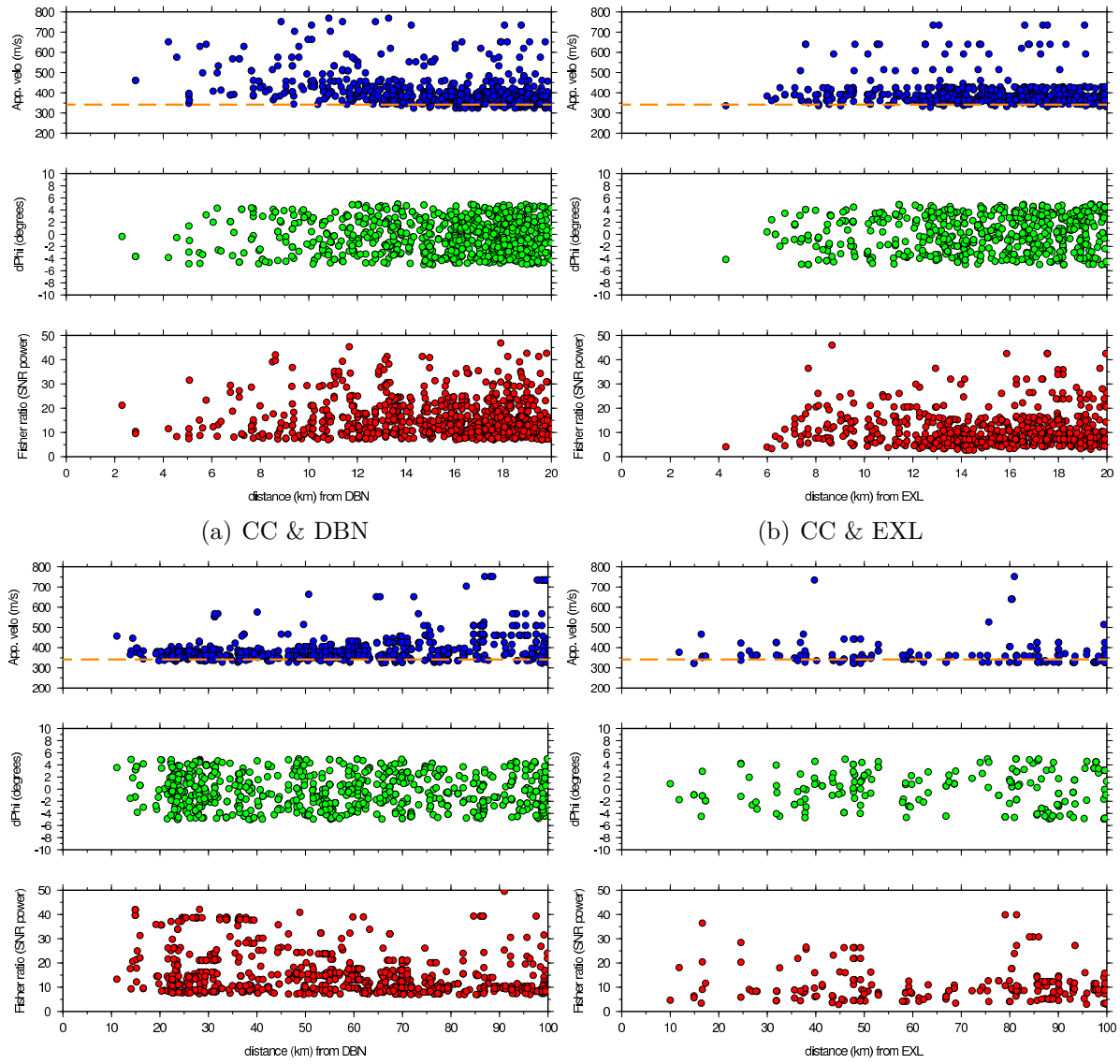

(a) CC & DBN

(b) CC & EXL

(c) CG & DBN

(d) CG & EXL

Figure 4.1.1: Statistical relations between distance of FLITS discharge detections to infrasound array and infrasound parameters. Considered infrasound parameters are Fisher ratio (S/N power ratio), back-azimuth deviation and apparent velocity. The orange dashed line is an estimated value of the speed of sound and equals 344 m/s.

sociations. Moreover, the amount of associated detections (normalized for area) increases with distance, which is not probable at all. For CG, the amount of associations decays with distance (see figure 4.1.2). Again, the relation between CC and Fisher is very poor and thus probably biased by misassociations. This stresses the point again that observed infrasound is associated to CG discharges best. Because of the poor relation, other infrasound parameters will not be discussed further for the CC plots.

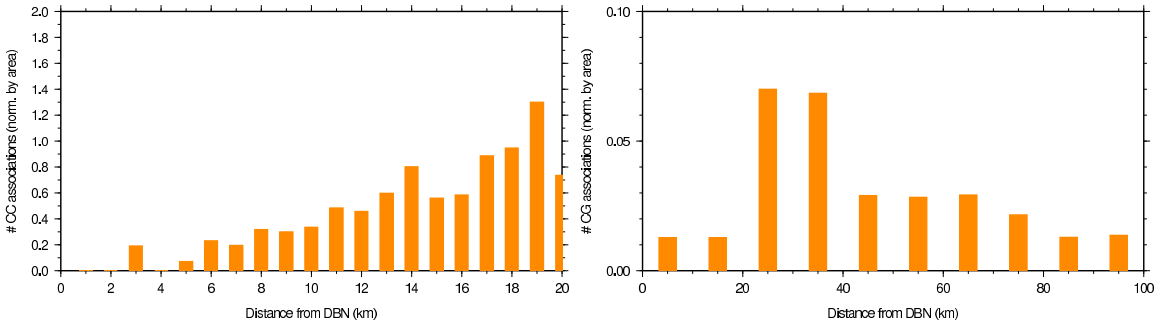

(a) CC associations at DBN

(b) CG associations at DBN

Figure 4.1.2: The amount of associations as function of distance to the infrasound array. The number of associations are normalized for the area of observation, since the area (and hence 'the probability') in which events can get associated increase with increasing distance from the infrasound array. Normalization will counteract this. The increasing amount of associations with distance for CC indicates that the statistics contain many misassociations since this is not energetically feasible. For CG, a likely decaying trend is observed.

It is remarkable that nearby discharges (up to 10 km) are not to be associated with infrasound detections, in this statistical representation. As a possible explanation, consider the state of the atmosphere during a thunderstorm. The highly convective nature of the atmosphere causes that nearby thunderstorm related infrasound get distorted very much and appear to be coming from different directions. The infrasound arrays are therefore expected to be 'deaf' for nearby discharges and misinterpretate the event's source. Therefore, there will be no correlation between FLITS and infrasound detections.

The deviation in back-azimuth statistics do not provide with a clear relationship. This may be explained in terms of uncertainties of a detection. The uncertainty is probably too high to resolve a certain trend within the small band of allowed deviation. However, by enlarging the band, the infrasound detections may be associated to FLITS detections falsely. This is an undesirable effect, therefore the deviation band is limited to be of 10°.

Lastly, an interesting relation between apparent velocity of infrasound and distance of the discharge to the array is observed for CG discharges. Especially at DBN, the apparent velocities increase with distance from the array. Apparent velocity values are higher for small distances as well. A similar behaviour is observed at EXL, but not so clearly, probably because of the lack of data. As a possible explanation, a raytracing study is presented in the next paragraph.

4.1.5 Raytracing as explanation for observed relation apparent velocity-distance

In order to explain the observed increase in apparent velocity with distance of the source for CG statistics, raytracing is performed in order to provide a possible explanation. Infrasonic raytracing is presented in *Garcés et al.* (1998) and is applied successfully in *Petit* (2000) in order to compare detected and calculated arrival times at DIA. In order to perform raytracing succefully, atmospheric models are required; data is provided by KNMI for specific dates at various moments in time. The models provide information on sonic velocities and winds as function of height. These atmospheric parameters determine the effective velocity at specific atmospheric heights, thereby creating a layered atmosphere through which the infrasonic waves travel and refract. Because of the directionality of winds, the velocity structure is different for specific azimuths, directions of wave propagation. Effective velocities are calculated by equation 4.1.1, as given by *Garcés et al.* (1998):

$$v_{eff} = \sqrt{\gamma_g RT} + \bar{n} \cdot \bar{u} \tag{4.1.1}$$

In which γ_g is the ratio of specific heats, R is the gas constant, T is the absolute temperature and $\bar{n} \cdot \bar{u}$ is the wind vector projection in the direction of wave propagation. As an adequate value, $\gamma_g R$ equals 402 $m^2/s^{-2}/K^{-1}$. Example calculations are given in the top window of figure 4.1.3; the green curve represents the effective velocity and the red curve is the thermal contribution to v_{eff}. The blue curve represents the speed of sound at the Earth surface and is plotted to show the contrast with the effective velocity.

Raytracing results are presented in figure 4.1.3; an atmospheric model for 2006-10-01 12:00 UTC is used. The source is modelled at 0 km height, propagates with 50° azimuth and with a launch angle of 0 to 90° from the Earth's surface. The source height and launch angle choices are based on CG source model assumptions, the selected azimuth is arbitrary. In the lower window of figure 4.1.3, rays are plotted with a interval of 1° in order to provide insight in the raypaths.

Figure 4.1.3 shows the different phases through the modelled troposphere; each phase has its distinct raypath. It is observed that with increasing distance, only phases returning from greater heights arrive. After an x amount of reflections at the Earth surface, the phase is believed to be non-existent. Furthermore, layers of contrasting velocities are visible, refraction will occur at each interface. The corresponding velocities are given by the scale to the right. Actually, the lower troposphere has a quite homogeneous velocity structure, considering the small variance of velocities in the figure.

It is important to note from this figure that with increasing distance from the source, more arriving phases will be from greater return heights. Therefore, it is to be expected that with increasing distance, the apparent velocity value will increase; this corresponds well with the observed statistics in figure 4.1.1. The increase of apparent velocity is more clearly plotted in figure 4.1.3b. Near the source, higher apparent velocity values are modelled as well, thereby predicting vertical incidence near the source.

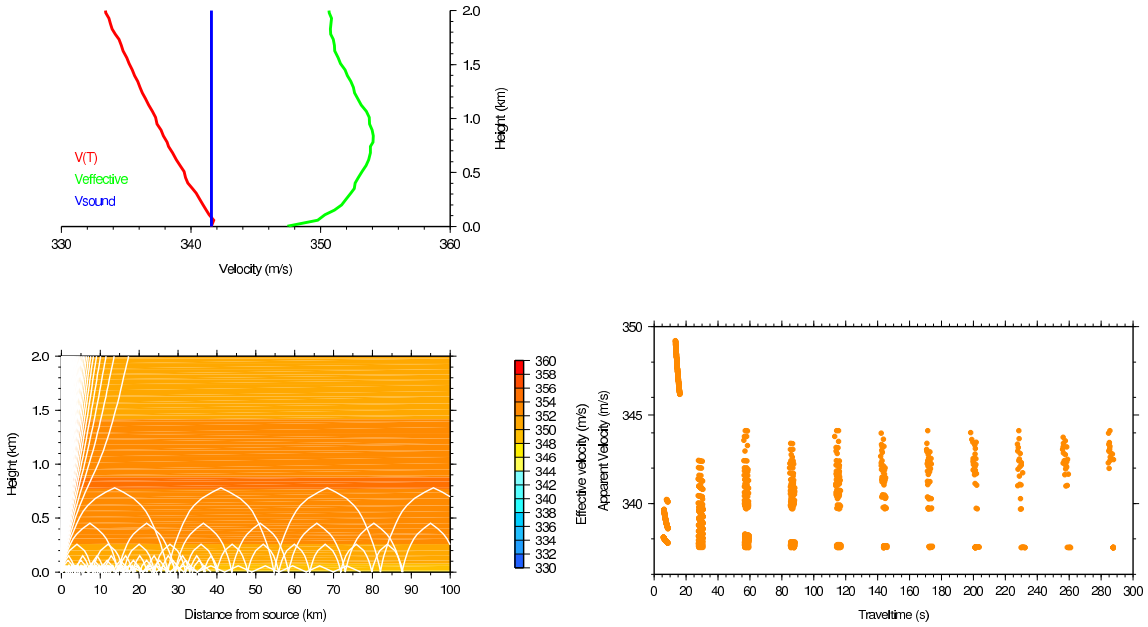

(a) Raypaths vs. distance

(b) Apparent velocity vs. traveltime

Figure 4.1.3: Raytracing results, using a KNMI Radiosonde measurement of the atmosphere for 2006-10-01. Figure **(a)** shows raypaths for raypropagation to 50° azimuth. Figure **(b)** shows the apparent velocity value for an arrival at traveltime t. At small and large traveltimes (= distances), apparent velocities higher than the speed of sound are modelled, possibly explaining the statistical relation in figure 4.1.1.

These results do not yet explain the much larger apparent velocity values from figure 4.1.1, at large distances. It might however be a step towards an adequate explanation. On the other hand, the statistics of CG may be biased as well by misassociations. However, because a proper correlation between Fisher ratio and distance exists and relations are similar for observations at both DBN and EXL, the argument for bias is easily rejected.

4.2 Content and behaviour of observed infrasound

4.2.1 Infrasonic waveform

In sections 3.1.1 and 3.2.1 clear multiple blastwave signatures are observed on the array traces for times of nearby thunderstorm activity. These blastwaves can easily be associated with CG discharges. A recording of an explosion by the DBN infrasound array is given in figure 4.2.1 and shows the behaviour of a blastwave. The waveform can be heavily influenced by meteorlogical conditions.

Together with the infrasound detection parameter apparent velocity, the observations on waveforms are important keys in understanding the source mechanism of infrasound generation by thunderstorms. Up till now, a clear relationship between CG lightning discharges and infrasound detections is presented, by comparing acoustic and electromagnetical detection mechanisms, in contrast to findings by *Beasley et al.* (1976). For infrasound which is readily associated to lightning, it is observed that relations exists between distance of the discharge and coherency, amplitude and apparent velocity of the infrasound signal. Especially the relation between distance and apparent velocity points out that infrasound from nearby thunderstorms is more vertically incident, while incidence is horizontally for thunderstorms further away. This relation considers direct phases; for refracted phases, the inverse relation may be true, as discussed in the preceding section on raytracing. In this study, infrasound is recorded from distant thunderstorms and can be readily associated to CG discharges; the associated waveform has the characteristics of a blastwave. As a source mechanism, the thermally driven expanding channel mechanism as proposed by *Few* (1969) explains the waveform.

These results appear to be in sharp contrast with findings from *Bohannon et al.* (1977); *Balanchandran* (1979) and the source mechanism proposed by *Dessler* (1973). These authors observe rarefaction waveforms, vertical incident on the array. Moreover, the observed waveforms show low coherency over the array elements. Thereby, it is stated that no infrasound is recorded from thunderstorms not overhead the array. In this study, the rarefaction pulse seldomly comes across on the array elements. However, by closely examining the waveforms around the time the thunderstorm is very near to DBN array, a symmetrical rarefaction pulse similar to the pulses presented in *Bohannon et al.* (1977); *Balanchandran* (1979); *Dessler* (1973) is observed at one of the array elements, DBN3 (see figure 4.2.2). The rarefaction is more dominant than compression, the signal frequency is ca. 0.5 Hz. In time, the pulse is between a sharp pulse and a wavetrain of blastwaves. The sharp pulse is observed and described earlier as a possible discharge on the array elements, because

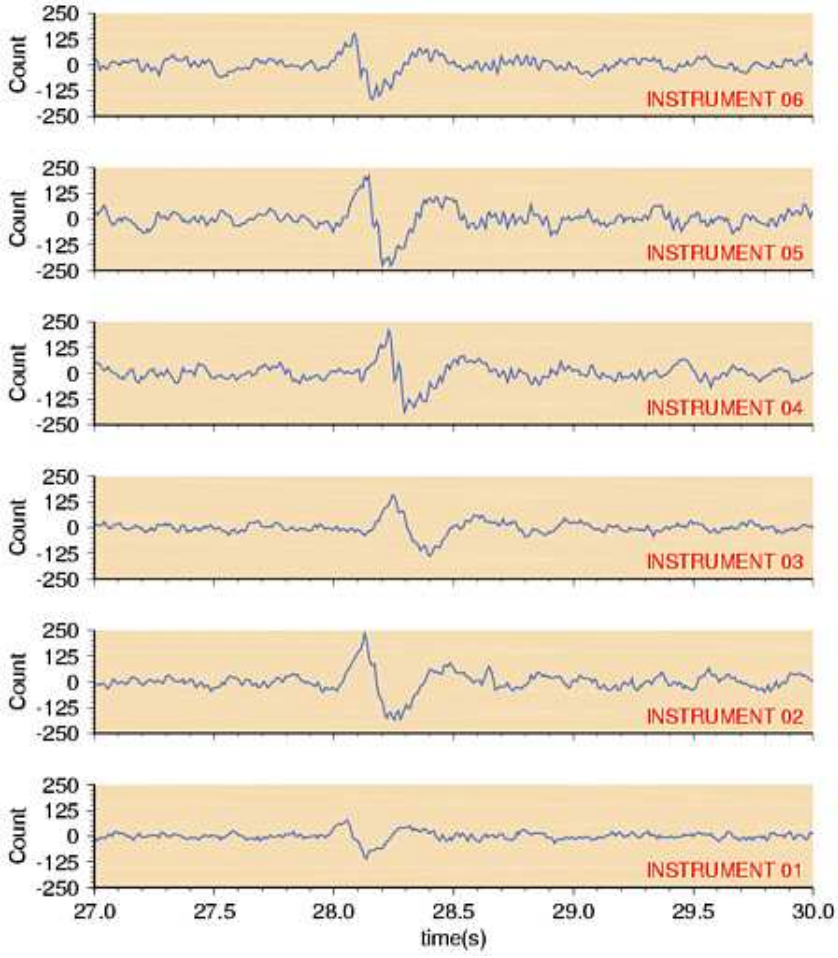

Figure 4.2.1: Recording of an explosion, measured at DBN. Note that all of the characteristics of blastwaves are present: an initial rise, a pressure drop, overshoot and the return to equilibrium. The differential traveltimes over the array elements give insight in the whereabouts of the event. Figure adapted from L.G. Evers.

of absent traveltime and occuring polarization differences. The rarefaction pulse is not observed on the other array elements; the lack of coherency will cause that the Fisher detector probably will not detect this event.

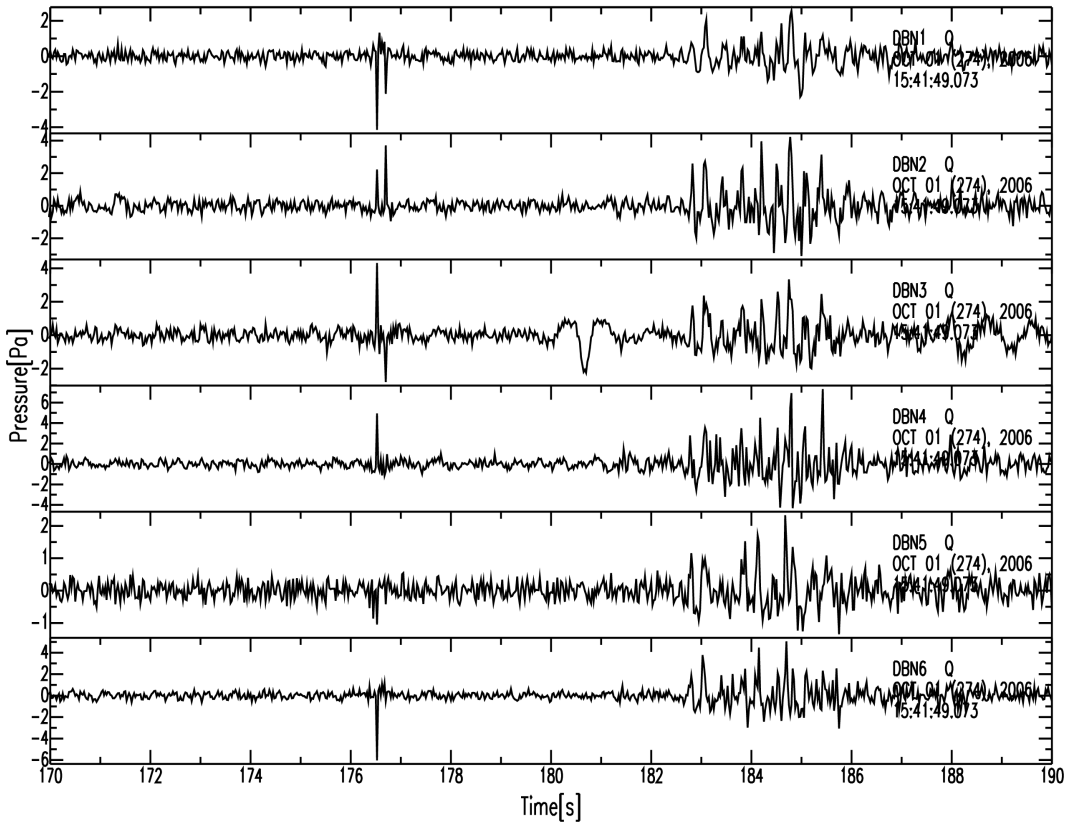

Figure 4.2.2: Infrasound recordings at 2006-10-01, around 13:44 UTC. On array element DBN3, a clear signature of a rarefaction pulse is observed around 180.5s, in between a peaked signal and a wavetrain of blastwaves. The peaked signal is a discharge on the array elements, the wavetrain is likely due to CG discharges. The single rarefaction pulse might be due to a CC discharge.

The electrostatic source mechanism model is successful in generating suchlike rarefaction pulses in the frequency range of 0.2-2 Hz. Power spectrum studies by *Few* (1969); *Holmes et al.* (1971) have shown that CC discharges have lower peak freqencies than CG discharges; *Holmes et al.* (1971) points out that CG discharges are readily explained by the mechanism as proposed by *Few* (1969), while CC discharges are to be explained by the electrostatic mechanism, as modelled by *Dessler* (1973). Similar frequency dependencies for CC and CG discharges are observed in this study, e.g. in figure 3.1.1a. For nearby CG discharges, the spectral peak increases up till 10 Hz, while spectral peaks are down to 2 Hz for thunderstorm activity with nearby CC discharges only.

The observations presented in this study support the conclusions from *Holmes et al.* (1971) and show that the operating infrasound arrays are able to associate detections

to CG discharges, based on the coherent blastwave travelling over the array elements. CC discharges on the other hand are not readily associated with infrasound detections. A possible explanation may be that observed incoherent rarefaction pulses are to be associated with CC discharges, in accordance with *Bohannon et al.* (1977); *Balanchandran* (1979); *Dessler* (1973). Lack of coherency will cause unsuccessful Fisher detections. Indeed, the predicted beam by the electrostatical mechanism is relatively restricted to straight down, as stated by *Dessler* (1973); therefore it could be incoherent over array elements. On the other hand it is doubtful that the signal is not detected on a 20 m distant array element; the rarefaction event could therefore be associated to other, very local events (e.g. winds) as well. Therefore, no further conclusions on CC associated waveforms should be drawn until further studies will sort out the likelihood of association of CC discharges to rarefaction pulses.

4.2.2 Attenuation of the waveform

In section 3.5, it is shown that the amplitude of associated infrasound decays with increasing distance from the source to the infrasound array. This relation is established using a variety of assumptions. It is important to discuss these assumptions and the shortcomings of the current method. Furthermore, the results are to be discussed in terms of attenuation and source mechanisms.

First of all, the association of infrasound to heavy lightning CG discharges measured by the FLITS network is carried out by assuming direct wave propagation through the lower troposphere. Because infrasound travels slower than electromagnetic waves, an infrasound arrival for a specific discharge is predicted by taking into account an estimate for the speed of sound. This predicted arrival is used to search the waveform for blastwaves near the predicted arrival time. Blastwaves are associated to lightning discharges only when a real arrival differs less than 5 s from the predicted arrival.

Furthermore, the amplitude of the first peak is picked for the associated blastwave for all array elements. The final value is an average over all picked values. This procedure is carried out for a large list of CG discharges. Since the first peak is not always clearly visible in the waveform, it could be an improvement to pick the well-developed trough, a ratio between peak and trough or even the energy of the whole blastwave.

The average amplitude value is furthermore normalized for the 'size' of the discharge. Hereby, it is assumed that the maximum value of measured current by FLITS is an appropriate measure of the size. Another, more physical measure could be the electrical current integrated over rise and decay time. Lastly, by normalizing, it is assumed that a linear relationship exists between the amplitude of associated infrasound and size of the discharge. In the end, the normalization is carried out since one wants to compare amplitudes for different sized discharges at different discharges. By normalizing for size, this dependency is assumed to be eliminated from the amplitude value.

Attenuation is the reduction in amplitude of a signal by transmission of the signal through a medium. Energy is dissipated basically because of geometrical spreading and the absorbing properties of the medium, because of which wave energy is converted to heat.

In seismology, the latter factor is often referred to as Q (Quality factor, $Q \propto \frac{1}{attenuation}$; see *Sheriff and Geldart* (1995). In discussing the results from figure 3.5.1, it is important to distinguish effects related to Q and effects related to geometrical spreading.

In figure 3.5.1, a decaying trend of normalized amplitude as function of distance to the infrasound array is visible. The nature of decay is of importance when interpreting the results in terms of attenuation mechanisms. The relation attenuation-distance is dependent on the mechanism of attenuation. Signals attenuate exponentially by transmission through a medium, while attenuation by geometrical spreading is described by an inverse law with distance. The exact inverse relation is determined by the nature of the source and the type of propagation. In discussing the results, it is assumed that the waves follow a direct path. For a point source, it can be shown that signals attenuate $\propto \frac{1}{r^2}$, while for a line source this is $\propto \frac{1}{r}$.

Atmospheric attenuation is modelled by *Volland* (1982); several atmospheric attenuation mechanisms are incorporated. These include molecular viscosity, heat conduction and molecular attenuation. The attenuation function as given by *Volland* (1982):

$$\delta P = \delta P_0 e^{-\alpha x} \tag{4.2.1}$$

δP is the differential pressure at distance x from the source, δP_0 is the differential pressure level nearby the source. α is the attenuation factor, and is given by:

$$\alpha = \frac{\omega^2 \tau}{2c} \tag{4.2.2}$$

In which ω is the angular frequency, τ is the relaxation time for the included attenuation mechanisms, and c is the speed of sound. In modelling, $\omega\tau << 1$. This value is suited for severe atmospheric conditions. Because $\omega\tau << 1$ results in a low α value, atmospheric attenuation is predicted to be negligible for frequencies < 100 Hz.

Assuming that atmospheric attenuation is indeed negligible for infrasonic waves, the presented results are more likely to be explained in terms of geometrical spreading. Therefore, the results are replotted in a log-log plot, in order to investigate a inverse law relation in the form:

$$\frac{Amplitude}{Current} ratio = \frac{k}{R^b} \tag{4.2.3}$$

In this relation, k is the inverse law constant. R refers to the distance of the source to the receiver and b corresponds to the nature of the inverse law. Since the form of the inverse relation corresponds to the type of source (point, line source), a suchlike analysis of the data in terms of geometrical spreading could result in a statement of the source type as function of distance. In order to do this, data is replotted in log-log plots in figure 4.2.3.

Figure 4.2.3a shows the data as presented in figure 3.5.1 in log-log plot. A more or less linear decrease is observable, although the points are scattered very much around the line. By assuming the inverse law relation, as given in equation 4.2.3, and by taking k to be equal to 50, the relation of b versus R is given in figure 4.2.3b. With increasing R, an decrease in b is observed.

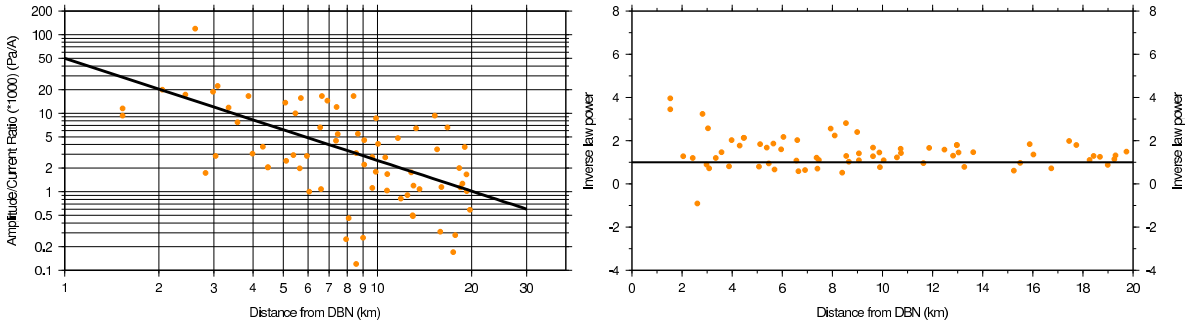

(a) Log-log representation of figure 3.5.1

(b) Inverse law analysis

Figure 4.2.3: Attenuation relation for associated infrasound. The orange dots represent the datapoints. In figure (a), figure 3.5.1 is replotted in a log-log plot. On top of the datapoints, geometrical spreading relation $\frac{k}{R}$ is given with a solid line. The line with $b = 1.3$ and $k = 50$ fits the data best. In figure (b), inverse law parameter b is plotted as function of R with $k = 50$. A solid line with $b = 1$ is plotted on top of the figure.

The value of b decreases until a value of $b = 1$ is reached; this is however dependent on the value of k, since this parameter translates the relation vertically. k is set by considering the best fit line in figure 4.2.3a. The results can be explained using the thermally expanding lightning channel model for CG discharges, as proposed by *Few* (1969). In this model, geometrical spreading of CG discharges is explained in terms of both spherical and cylindrical spreading, for near- and far-field locations respectively. Considering these results, the b value acts as a predictor of the acting spreading mechanism. For nearby CG discharges, high b values point to point-source (spherical) divergence; further away the divergence changes to line-source (cylindrical) divergence, as indicated by the lower inverse power values around $b = 1$.

However, in future studies, advanced boundary conditions should be considered and a larger dataset should be used in order to investigate the relation further, since the spread in figure 3.5.1 is still very large. Whether atmospheric attenuation (Q) is really negligible could be investigated further and one could focus on the propagation path of infrasonic signals from lightning.

4.3 Comparison and verification FLITS network

In this study, infrasound detections have been compared with detections from a lightning detection system based on electromagnetic waves. Overall, good agreement is found between directions of CG lightning discharges and directions of coherent infrasound. Moreover, relations between spectral content, amplitude, apparent velocity and coherency of the signal on the one hand and distance of the CG discharges to the infrasound array on the other hand are very promising. Lastly, associated infrasound to CG discharge has the very distinct waveform character of a blastwave. The blastwave is coherent over all array

elements, causing successful detection. Detections on single arrays however do not provide with localizations of discharges. Infrasound detections are not in good agreement with directions of CC lightning discharges. Although observed incoherent rarefaction pulses could possibly be related to CC discharges overhead the infrasound array, no conclusions are drawn in the association of CC discharges to infrasound. Future studies should sort this out.

The current infrasound array network in The Netherlands is unable to provide localization using crossbearing, probably because of the long distances between the arrays. The nearest array to DBN, DIA, is yet unable to detect CG lightning discharges adequately. Future developments may enable lightning discharge detection at DIA, such that it can be investigated whether crossbearing results are fruitful. Moreover, the detection algorithm may be tailored further to exploit the characteristic waveform of CG discharges.

Thus, although single array detections are in good agreement with discharge detections from the FLITS network, ambiguity in detections still plays a role. Because of this, the infrasound network is up till now not able to validate the detection results obtained by the FLITS network. An important next step in these studies is the successful unambiguous localization of lightning discharges by infrasound arrays.

In *Holleman et al.* (2006), validation of the FLITS system was presented as a pilot study. As validation techniques, weather radar, infrasound and LOFAR telescope were exploited. Weather radar results enable validation of the FLITS network; a false-alarm ratio of 0.010 is obtained for 2004. The probability of detection, i.e. the probability that a real lightning discharge is detected by the lightning detection network, is not to be determined using weather radar. This is because weather radar does not measure lightning detections directly; the measured property is radar reflectivity and reflectivity proves to correlate well with locations of FLITS detections. This is because radar reflectivity is a measure of strength of convection and moist in the air; two main drives behind lightning activity.

Furthermore, it is shown that LOFAR validates FLITS detections in time and space. Moreover, the number of observed events is larger for LOFAR detections. It is expected that the telescope will contribute in the monitoring of lightning discharges. Because of denser network coverage and higher signal sampling, a more precise spatial-temporal evolution of radio-emissive processes in a thunderstorm is expected.

In this study, validation of the FLITS network using infrasound is investigated further. As mentoined, promising relations exist between FLITS CG discharges and measured infrasound at single arrays, but associating detections at multiple arrays is yet a bridge too far. Therefore, providing that crossbearing localization is successful in the future, validation of CG lightning discharges is expected to be possible. Moreover, infrasound is a way to measure discharges directly, in contrast with weather radar. Validation of the FLITS network with infrasound will therefore provide with estimates on false-alarm ratio's and probability of detections.

In conclusion, enough possible research objectives to pursuit the validation of the FLITS system further. Although the FLITS system appears to provide thrustworthy results w.r.t. lightning detection, validation studies show that improvements in lightning detection are

nevertheless possible.

4.4 Subsonic events

Apart from infrasound event detections, infrasound arrays appear to be able to resolve the whereabouts of subsonic thunderstorm fronts perfectly. The pressure signature of these fronts is well known in meteorology, see for example *Wessels* (1964). On the array microbarometers, a very clear drop in pressure is observed. Because of the shape of the pressure drop, the front is often referred to as thunderstorm 'nose'. The drop might be so large that the signal is clipped.

Observations on thunderstorm noses show that the propagation direction of the subsonic disturbance coincides with the direction in which the thunderstorm evolves. The nose is very coherent over all array elements; since it is a macro scale feature, this is quite logical. The high coherency results in high Fisher ratio's. Thunderstorm fronts travel with the speed of local winds. Infrasound array measurements resolve velocities in the range of 10-20 m/s, as presented in figure 3.4.1.

Whether the observed noses at DBN and DIA can be related, depends on the differential traveltime. Consider figure 3.4.1. For the first observed nose at DIA, the differential traveltime would equal 19 minutes. Assuming a distance of 55 km between DBN and DIA, 19 minutes corresponds to an apparent velocity of 48 m/s. Considering an back-azimuth of 240°, the true velocity would equal 38 m/s. This is relatively high. For the second nose observed at DIA, the differential traveltime would equal 34 minutes, corresponding to a true velocity of 22 m/s. This value for true velocity appears to be more truthful.

At DIA, the pressure level of the associated nose is decreased w.r.t. the nose at DBN (-10 Pa vs. -35 Pa). A lowering in thunderstorm intensity could explain this feature. Since the storm evolves from Southwest to Northeast, the nose first encounters DBN and DIA later in time.

In conclusion, observations at infrasound arrays on subsonic pressure disturbances can be used to monitor evolving storms.

Chapter 5

Conclusions

By comparing infrasound detections with lightning discharge detections, the following results are obtained:

- FLITS CG lightning detections are well correlated in time with coherent infrasound detections up to 70-80 km distance. A clear relation exists between the distance of CG discharges to infrasound arrays on the one hand and spectral content, amplitude, apparent velocity and coherency of the infrasound on the other hand.
- Infrasound records show clear marks of blast-waveforms, associated to CG discharges. As a source mechanism, the *thermally expanding lightning channel model* appears to be appropriate.
- Attenuation is observed for associated blast-waveforms; although the current dataset shows a decaying trend, the scattering in datapoints is still very large. From theory, atmospheric attenuation (Q) is regarded to be negligible. Results can be explained in terms of geometrical spreading.
- Infrasound detections appear to be sensitive to meteorlogical conditions; wind direction and temperature are important parameters in wave propagation paths.
- Single array detections offer very good, but possibly ambiguous detection results; the current infrasound network is unable to detect discharges unambiguously by cross-bearing localization. Therefore, validation of the FLITS network using infrasound arrays is yet not possible.
- Infrasound arrays detect subsonic thunderstorm fronts adequately and provide information on the direction of the storm fronts. Hereby, the evolution of storms can be monitored.

Future studies may focus on:

- Exploiting the blast-waveform in an algorithm to detect CG lightning discharges even more accurately or at larger distances. This will increase the ability of the infrasound array network to detect lightning discharges.
- Improved attenuation studies: advanced boundary conditions (e.g. waveform energies instead of amplitudes) and a larger dataset to reduce the variance obtained in the current relation. On basis of these results, improved experimental attenuation relations can be formulated and can be compared with theory to investigate atmospheric attenuation and geometrical spreading further.
- Further crossbearing localization studies by improving the detection of discharges at DIA. Because DIA is closer to DBN than EXL, it is to be expected that successful detection of discharges at DIA will also lead to successful crossbearing localization and thus a validation for the FLITS network.

Acknowledgements

My Master's research project and thesis have come to an end. Therefore, I would like to express my gratefulness in this last section of my thesis.

First of all, I would like to thank Läslo Evers for being such a fantastic supervisor. Especially our non-formal style of discussions, both at KNMI and during our frequent drinks at 'Binnenbest' definitely account for the good atmosphere. You are not merely a gifted and creative scientist, you are also able to share your knowledge with fellow workers in a very practical and structural way. I am sure we will keep in touch and occasionally will return to 'Binnenbest'. Good luck in writing your symphony!

Furthermore, I would to thank Hanneke Paulssen for being my supervisor at Utrecht University. Your critical views and comments definitely improved the study. Although you seem a bit reserved at first sight, you really have a warm personality and I enjoyed working together with you very much, as during my Bachelor research.

From the Weather Research department, I would like to thank Iwan Holleman, for the pleasant cooperation. Although we did not meet very often, your input really improved the results and discussion, especially towards the end of the study.

Many, many thanks to everybody from the KNMI Seismology department, for the pleasant atmosphere during my job and research project. I really have had a good time with all of you. Special thanks to Rik, for introducing me to the department and Quintijn and Ylona for working together with me so pleasantly. I definitely will miss our room at the top! Furthermore, a special word to my (infrasound) partners in crime, Johan, Tim and Gert-Jan. Thanks for all interesting discussions, you really supported me during my research. Good luck during yours!

Furthermore, I would like to thank all my study friends, the U.G.V. boards and especially my fellow, rock-solid board members of the 59th board. A special word to Koen, Mara and Menne for friendship and interesting discussions.

Thanks to all my roommates at WB53, to all 'Deltamossels' for the good atmosphere at our house! I really will miss you lot while living in London!

Lastly, all my gratefulness to my parents, to my sister Eva and to Arnold for being such a loving family.

Bibliography

Balanchandran, N.K., Infrasonic Signals from Thunder, *J. Geophys. Res.*, vol. 84, no. C4, pp. 1735-1745, 1979

Barthendu, Comments on "On the Power Spectrum and Mechanism of Thunder", *J. Geophys. Res.*, vol. 76, no. 30, pp. 7441-7442, 1971

Beasley, W.H., Georges, T.M., Evans, M.W., Infrasound From Convective Storms: An Experimental Test of Electrical Source Mechanisms, *J. Geophys. Res.*, vol. 81, no. 18, pp. 3133-3140, 1976

Bedard Jr., A.J., Low-Frequency Atmospheric Acoustic Energy Associated with Vortices Produced by Thunderstorms, *Monthly Weather Review*, vol. 133, pp. 241-263, 2005

Bohannon, J.L., Few, A.A., Dessler, A.J., Detection of infrasonic pulses from thunderclouds, *Geophys. Res. Let*, vol. 4, no. 1, 1977

Bowman, H.S., Bedard, A.J., Observations of Infrasound and Subsonic Disturbances Related to Severe Weather, *Geophys. J. R. astr. Soc.*, vol. 26, pp. 215-242, 1971

Calje, L., Exploring boundaries of the Fisher and PMCC signal-detectors using infrasound signals, *Utrecht University MSc Thesis*, 38 pp., 2005

Cansi, Y., An automatic seismic event processing for detection and location: The P.M.C.C. method, *Geophys. Res. Letters*, vol. 22, no. 9, pp. 1021-1024, 1995

Dessler, A.J., Infrasonic Thunder, *J. Geophys. Res.*, vol. 78, no. 12, pp. 1889-1896, 1973

Evers, L.G., Haak, H.W., Listening to sounds from an exploding meteor and oceanic waves, *Geophysical Research Letters*, vol. 28, no. 1, pp. 41-44, 2001

Evers, L.G., Haak, H.W., Tracing a meteoric trajectory with infrasound, *Geophysical Research Letters*, vol. 30, no. 24, 2003

Evers, L.G., Haak, H.W., The detectability of infrasound in the Netherlands from the Italian volcano Mt. Etna, *Journal of Atmospheric and Solar-Terrestrial Physics*, vol. 67, no. 3, pp. 259-268, 2005

Evers, L.G., On the detection of infrasound in the atmosphere, *Delft University PhD thesis, in prep.*

Few, A.A., Power Spectrum of Thunder, *J. Geophys. Res.*, vol. 74, no. 28, pp. 6926-6934, 1969

Fisher, R.A., Statistical methods for research workers, *Oliver and Boyd*, London, 1948

Garcés, M.A., Hansen, R.A., Lindquist, K.G., Traveltimes for infrasonic waves propagating in a stratified atmosphere, *Geophys. J. Int.*, vol. 135, pp. 255-263, 1998

Holleman, I., Beekhuis, H., Noteboom, S., Evers, L., Haak, H., Falcke, H., Bähren, L., Validation of an operational lightning detection system, *2006 ILDC/ILMC Validation of Operational LDS*, 32pp., 2006

Holleman, I., Handboek Waarnemingen, Hoofdstuk 20, Bliksem, *KNMI Handboeken*, 31 pp., 2005

Holmes, C.R., Brook, M. Krehbiel, P., McCrory, R., On the Power Spectrum and Mechanism of Thunder, *J. Geophys. Res.*, vol. 76, no. 9, pp. 2106-2115, 1971

Holmes, C.R., Brook, M. Krehbiel, P., McCrory, R., Reply on "On the Power Spectrum and Mechanism of Thunder", *J. Geophys. Res.*, vol. 76, no. 30, pp. 7443, 1971

Liszka, L. Hobara, Y., Sprite-attributed infrasonic chirps - their detection, occurrence and properties between 1994 and 2004, *J. of Atmospheric and Solar-Terrestrial Phys.*, vol. 68, pp. 1179-1188, 2006

Melton, B.S., Bailey, L.F., Multiple Signal Correlators, *Geophysics*, vol. 22, no. 3, pp. 565-588, 1957

Noble, J.M., Passner, J.E., Infrasound monitoring of severe storms, *unpublished*

Noteboom, S., Processing, validatie en analyse van bliksemdata uit het SAFIR/FLITS systeem, *KNMI rapport*, 71 pp., 2006

Petit, M.E., Infrasonic wave propgation through the atmosphere, *Utrecht University MSc Thesis*, 42pp., 2000

Sheriff, R.E., Geldart, L.P., Exploration Seismology, *Cambridge University Press*, 592pp., 1995

Smart, E., Flinn, E.A., Fast Frequency-Wavenumber Analysis and Fisher Signal Detection in Real-Time Infrasonic Array Data Processing, *Geophys. J. R. astr. Soc.*, vol. 26, pp. 279-284, 1971

Volland, H., Handbook of atmospherics, *CRC Press, inc*, pp. 275-278, 1982

Wessel, P., Smith, W.H.F., Free software helps map and display data, *EOS Trans. AGU*, vol. 72, pp. 441, 1991

Wessels, H.R.A., Het noodweer van 18 juli 1964, *KNMI publicatie*, pp. 132-139, 1964